Combined effect of a spread powder particle size distribution, surface machining and stress-relief heat treatment on microstructure, tensile and fatigue properties of 316L steel manufactured by laser powder bed fusion

Josiane Nguejio[a], Morgane Mokhtari[a,b], Elie Paccou[a], Eric Baustert[c], Leila Khalij[d], Eric Hug[e],, Pierre Bernard[f], Sébastien Boileau[g], Clément Keller[a,b,*]

[a] Univ Rouen Normandie, INSA Rouen Normandie, CNRS, Groupe de Physique des Matériaux UMR 6634, F-76000 Rouen, France

[b] Laboratoire Génie de Production, ENIT-INP, avenue d'Azereix, 65000 Tarbes, France

[c] Volum-e, Rue de la fonderie, 76340, Blangy-sur-bresle, France

[d] Laboratoire de Mécanique de Normandie, INSA-Rouen Normandie, avenue de l'Université, , F-76000 Rouen, France

[e]Laboratoire Crismat, UMR CNRS 6508, ENSICaen, Université de Caen, bvd du maréchal Juin, 14000 Caen, France

[f]ArianeGroup, Forêt de Vernon, 27200, Vernon, France

[g]Laboratoire Analyses et surface, Groupe 6napse, 2 voie de l'innovation 27100 Val De Reuil, France

* corresponding author: clement.keller@enit.fr

Abstract

Additive Manufacturing is a powerful process to build complex geometry. Besides the numerous process parameters influencing the mechanical part performances, others parameters related to the initial powder feedstock or component machining are of most importance. In this study, the combined effect of a wide particle size distribution, surface machining and stress-relief heat treatment on the microstructure and mechanical properties (tension and fatigue) of a stainless steel AISI 316L, produced by laser powder bed fusion, is investigated. In order to correctly investigate those parameters separately, the netshape/machined character of the sample, alongside with the heat treatment is studied for two kinds of powder having different particle size distributions, i.e, narrow and widely spread. Results show that a large spread of particle size is only slightly detrimental to the fatigue life, in particular in high cycle conditions due to a larger porosity related to a weakly more uneven particle spatial distribution in the bed. Nevertheless, this effect is of a second order compared to machining or heat treatments which greatly affect the mechanical behaviour. Surface machining and moderate heat treatment are then the best post-operational steps to increase the fatigue life in high cycle fatigue conditions independently of the particle size distribution. Results are discussed in terms of defects, microstructural modifications, surface roughness, martensitic transformation and mechanical loading.

Keywords:

Laser Powder Bed Fusion, stainless steel, powder characteristics, microstructure, fatigue, heat treatment, machining.

This is a postprint version of the published version of the article published in *The International Journal of Advanced Manufacturing Technology* (https://doi.org/10.1007/s00170-023-11008-w). Thanks to Springer to publish this article.

Introduction

AISI 316L (316L) is an austenitic stainless steel widely used in various industrial applications due to its corrosion resistance, mechanical properties and formability. Thanks to its good weldability, 316L parts can be also produced by Additive Manufacturing (AM) processes which enables the production of parts with complex geometries [1,2]. Among all AM processes suitable for 316L manufacturing, Laser Powder Bed Fusion (LPBF) is widely employed industrially and deserve attention.

Microstructures obtained by LPBF differs from those issued from conventional processes. Defects such as pores, lack of fusion or high dislocation densities can be observed [1] alongside with morphologic and crystallographic texture generally characterized as {101}<001> (goss)[3,4] or {001}<001> (cubic) [5,6]. The optimization of the manufacturing parameters such as laser power, laser speed, powder layer thickness, hatch distance and scanning strategy, can lead to a reduction in these defects [7–10]. Although process parameters are key factors to control the microstructure and induced defects such as pores, others parameters including, for example, build orientation and post-treatments also influence mechanical properties (e.g., ultimate tensile strength). For instance, vertical samples enable a higher elongation to fracture than horizontal samples due to the anisotropic microstructure [11,12]. An increase in the fatigue endurance from 20 to 50% has also been reported when removing netshape roughness by polishing or sample machining [11,13–17].

In order to improve the mechanical properties, several heat treatments have been designed and reported in the literature. Among them, for austenitic stainless steels, stress-relieving treatments (temperature in the range of 600-800°C) have been studied. Indeed, those annealing steps, which generally preserve the typical AM microstructure, lead to a decrease in their ultimate tensile strength (UTS) and an increase in their ductility when compared to as-built samples [18,19]. With regard to fatigue resistance, it seems that it could be slightly improved by a heat treatment [14,15], especially if residual stress reduction is involved. Nevertheless, a slight decrease in tensile mechanical properties has been also reported for that kind of heat treatment due to the intercellular precipitation of σ-phase (with higher Mo and Cr concentration) in the δ-ferrite/γ-austenite phases boundaries [12].

For powder bed fusion processes, powder control (chemical composition, particle shape, size and size distribution) is of prime importance. Industrially, different powder batches or different suppliers are employed for production purposes. This change from a batch/supplier to another may induce variations in powder characteristics which could lead to a change in the microstructure and mechanical part performance [20–22]. Furthermore, nowadays, cost and waste reduction in AM constrain industries to reuse the powder of a given batch which may affect the properties of the final parts [21,22]. Even if a sieving process is performed, the average particle size generally increases with powder reusing [23–27]. Concerning powder composition, an increase in oxygen content is sometimes reported [26,28–30]. In 316L, both phenomena have been observed, resulting in a decrease in part density and an increase in ductility [26] as well as an increase in surface roughness [27]. For IN718, the increase in particle size and oxygen content only slightly reduce the fatigue life associated to low plastic strain amplitude [31]. In that case, this reduction is due to the increase in particle size which modifies the powder flowability during the process [31]. The particle size distribution therefore seems to be one of the most influential parameters on the mechanical properties.

For 316L, the influence of the particle size distribution on part microstructure and mechanical properties has already been studied. It has been reported that even for powder batches presenting the same average particle diameter, the size distribution plays a role on the process and part quality [32]. The

authors claimed that wide particle size distribution (2-70 µm) gives a better tap/netshape density as well as a lower surface roughness whereas a narrow distribution (15-70 µm) results in a better flowability and a higher ultimate tensile strength [32]. A decrease in average particle size has been also reported to produce lower surface roughness [33] whereas an average particle size value above the range 28-38 µm leads to an increase in porosity [34]. An adaptation of the manufacturing parameters to particle size distribution has been also reported to ensure high density samples [35–37]. Furthermore, it was reported that optimal mechanical properties in tension can be obtained by mixing two particle populations (i.e. spread and narrow) [35,36].

Moreover, in some cases, small powder quantities remaining after jobs that cannot be used again, can be mixed all together to produce new parts. That kind of strategy can help to reduce powder wastes and makes LPBF process more efficient. In that case, the obtained row powder can exhibit a very wide spread particle size distribution (which does not fulfil common AM requirements) which may affect the part mechanical performances. It is then of prime importance to assess the impact of such powders on the part quality. In literature, the role played by a very wide particle size distribution on mechanical behaviour, especially in fatigue, was not properly addressed, either in Low Cycle Fatigue (LCF) or High Cycle Fatigue (HCF). Furthermore, AM samples are generally submitted to post-operational treatments such as machining or stress-relief heat treatments, which can change the conclusions regarding powder particle influence on mechanical properties. Considering the great interest in fatigue loadings in industry, this lack of knowledge can lead to incorrect industrial criteria for powder employability, resulting in higher economic and environmental costs.

The main objective of this study is then to better understand the role played by a very wide powder particle size distribution over a large range of microstructure characteristics and mechanical properties of samples manufactured by LPBF. For comparison purposes, two powders were employed to produce samples, one with a narrow particle size distribution (supposed to be optimal for LPBF) and a second one with a very large particle distribution. Those samples were subjected to different post-operational steps such as machining and stress relief heat-treatments. A particular attention was paid to the characterization of the fatigue properties in tension, compression and vibration bending to cover both elastic and plastic regimes which are of great industrial interest.

1. Manufacturing and sample description

The effect of the powder particle size distribution is investigated by using two different 316L powders: one with a narrow particle size distribution (labelled narrow powder in the following paragraphs) and the second one with a very wide size distribution (labelled spread powder in the following paragraphs). These precursor powders are both provided by the Erasteel company and will be fully described in section 3.

Sample manufacturing was performed by Volum-e company using an EOS M290 powder bed fusion machine, equipped with a continuous fiber laser and a maximum power capacity of 500W. The bulk printing parameters are given in Table 1. A contour strategy has been applied for all samples with two laser vectors (same hatch distance for bulk areas) and reduced laser power and speed (P=150 W, V=450 mm/s).

Table 1: Manufacturing parameters used on the EOS M290 employed in this study.

Laser power (W)	Laser scanning speed (mm/s)	Layer thickness (µm)	Hatch distance (mm)	Angle (°)
195	900	40	0.1	67

In order to investigate the role played by machining and surface roughness on the mechanical behaviour (static and fatigue), a total of four sample series were manufactured vertically from the two powders, narrow and spread one (for each powder type, all samples fit in one plate). For monotonic and conventional cyclic tests, the first series consists in samples built as cylinders of 20 mm diameter and 200 mm height for further machining (conventional turning) to obtain ISO 12106:2017 standard samples with a gauge length of 20 mm and diameter of 8 mm for a total length of 90 mm (two samples were machined in one cylinder). This first series will be called referred to as M. The second series is based on netshape samples manufactured with the same geometry as machined one. Samples from this series will be labelled NS.

The last two sample series are dedicated to vibration fatigue tests carried out with an electrodynamic shaker. For the netshape configuration, walls of 120x20x2 mm (L×l×t) were manufactured for both powders (samples will be designated NS_V; “V” standing for vibration). Finally, 120x20x20 mm blocks (L×l×t) were produced for further machining (electro-discharge machining) of samples with same dimensions as netshape ones. Samples associated to these series are called M_V.

For these two sample geometries, “N” and “S” suffixes are added to series names for narrow and spread powder, respectively. In order to characterize the influence of a stress relief heat-treatment on the mechanical properties, a part of M, M_V and NS_V series samples was heat treated at 720°C during 2h. This temperature is expected to belong to the transition between recovery and homogenisation treatments [5]. The suffix “HT” on the name sample refers to these heat-treated samples. To sum up the sample nomenclature, for instance, a netshape sample built from spread powder and then heat-treated prior to vibration mechanical testing is called NS_V_S_HT. Table 2 summarizes the different samples employed in this study, the precursor powder, netshape or machined conditions, together with the kind of applied mechanical loading and number of samples employed for each mechanical test. Finally, a specific sample including overhang walls oriented to 65 and 75° with respect to the building direction was also produced for each powder for surface roughness measurements.

Table 2: Summary of the different samples additively manufactured in this study and the associated mechanical loadings.

Sample Id.	State	Powder	Heat-treatment	Mechanical characterization				
				Tensile	CSSC	Conventional fatigue	Vibration fatigue	Sample number per loading
M_N	Machined	Narrow	no	yes	yes	yes	no	3
M_N_HT	Machined	Narrow	yes					
M_S	Machined	Spread	no					
M_S_HT	Machined	Spread	yes					
NS_N	Netshape	Narrow	no		no			
NS_S	Netshape	Spread	no					
M_V_N	Machined	Narrow	no	no	no	no	yes	3
M_V_N_HT	Machined	Narrow	yes					
M_V_S	Machined	Spread	no					
M_V_S_HT	Machined	Spread	yes					
NS_V_N	Netshape	Narrow	no					
NS_V_N_HT	Netshape	Narrow	yes					
NS_V_S	Netshape	Spread	no					
NS_V_S_HT	Netshape	Spread	yes					

Figure 1 illustrates the production plate manufactured from the narrow powder. For both netshape sample series, lateral reinforcements were employed to avoid bending in the case of contact between the solid body and the recoater. As the position of a sample in the plate can significantly affects its mechanical properties [38], in this study, as observed in Figure 1, the different samples of each series were placed as randomly as possible in the plate. In that case, any significant change in mechanical properties must be due to the powder characteristics or post-operational treatments and not to the sample position in the plate.

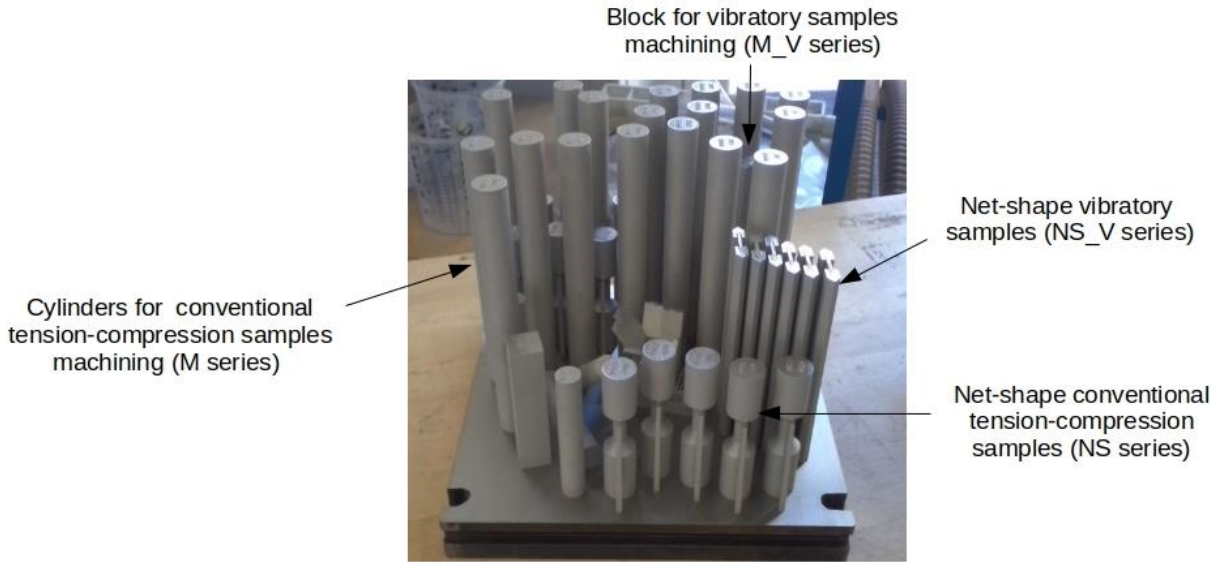

Figure 1: Illustration of a production job for the narrow powder on the EOS M290 LPBF machine.

2. Experimental methods

This work aims at investigating the effect of the powder particle size distribution with a large spread on the microstructure and mechanical properties. In order to correctly capture this effect, powders were first analyzed in terms of chemical composition and flowability. Then, a multi-scale microstructure investigation (density, surface roughness, phases, texture, grain size, dendrite, precipitation) on fused material was performed. Finally, the mechanical properties were assessed both in tension and fatigue. All methods employed for such investigation are described in the following subsections.

2.1. Powder analysis

Powder chemical composition was analysed by Inductively Coupled Plasma Optical Emission Spectroscopy - ICP-OES -, Glow Discharge Mass Spectrometry - GMDS - and Instrumental Gaz Analysis – IGA Inductively Coupled Plasma (ICP) depending of the chemical elements. A particle characterization system Malvern panalytical MORPHOLOGI G3 was also employed to assess the particle size distribution. Together with this analysis of the distribution of powder particle size, the conventional powder flowability was characterized using a standard flowmeter funnel (ASTM B213). The apparent density was also measured with the same flowmeter (ASTM B212) whereas the tap density was measured with a Densitap machine following ASTM B 527 standard. For a better characterization of the powder flowability, the avalanche energy, the break energy, the avalanche and rest angles were also measured using a rotating drum device (Mercury scientific).

2.2. Microstructure and surface roughness characterization

Melting pools, pores, dendrites, grain sizes and grain orientations were characterized using a Scanning Electron Microscope (SEM, JEOL 7900F) coupled with Electron Backscattered Diffraction (EBSD). Prior to the observations, all samples were polished up to a 1200 SiC paper. For SEM analyses, samples were then electropolished (30s, 20V, Lectropol-5, Struers) using a 73% ethanol, 10% glycol, 8% perchloric

acid and 9% water electrolyte. SEM-EBSD orientation maps were acquired with a 1 µm step with a high voltage of 25 kV. Data were analyzed with OIM software.

Samples used for Transmission Electron Microscopy (TEM) were taken from the mechanical testing samples in the initial or post-mortem state after mechanical loading. Foils were prepared by grinding coupons down to approximately 80 µm and then punched to obtain disks with a diameter of 3 mm. These disks were electropolished and thinned with a 10% perchloric acid solution in 90% methanol at -35°C and 20V using a twin-jet Tenupol-5.

The strain induced austenite → α'-martensite phase transformation was investigated by measuring the magnetic fraction (content of α'-martensite) in the sample gauge length using a magneto-inductive testing device (Fischer feritscope), before and after the fatigue tests. The final content of α'-martensite value was obtained by averaging data from twenty local measurements along the gauge length of each sample.

The relative densities were measured with an Archimedes type balance (with 0.1 g accuracy) using a reference value of 7.98 g/cm^3. This reference value was measured with the same method on a 316L stainless steel plate obtained by conventional manufacturing process. For each sample, an average of 5 measurements was performed in order to take into account the experimental scattering. In addition to those relative density measurements, porosity analysis was achieved after converting thirty micrographs into binary images using Fiji software [39]. Images were captured by means of a Keyence VHX-500 digital microscope at 200x magnification, leading to an image size of 1500×1160 µm size with a resolution of about 1.03 pixels/µm.

The surface roughness measurements were performed on Altimet© Altisurf 500 metrology station on a 2 mm^2 sample area with a 1 µm displacement resolution. The total length of the surface roughness profile was about 15 mm.

2.3. Mechanical testing procedures

Monotonic tensile tests were carried out on an electromechanical MTS C45 tensile machine controlled by a cross-head displacement. All tests were performed with a strain rate of about 1.7x10^{-3} s^{-1}, and the axial strain is measured using a "clip-on" extensometer (100% capacity).

Conventional cyclic mechanical behaviour was investigated with Cyclic Stress-Strain Curves (CSSC) and fatigue tests on an MTS servohydraulic machine with a load capacity of 100kN under a total strain amplitude control. The CSSC curves were performed to quickly identify the cyclic behaviour of each material over a wide region of plastic strain amplitudes. During the test, samples were subjected to a stepwise increase in the total strain amplitude from 10^{-4} to 10^{-2} every 250 cycles.

Fatigue tests were performed under strain control for 3 different total strain amplitudes corresponding to Low cycle fatigue (LCF), High Cycle Fatigue (HCF) and Medium Cycle Fatigue (MCF). These three total strain amplitudes give rise to plastic deformation. All cyclic tests were carried out with a symmetric tensile/compression loading (R=-1), at a frequency in the range 1-5 Hz leading to a strain rate of about (1.7±1) x10^{-3} s^{-1} (similar to tensile one). To consider experimental scattering, all conventional monotonic and cyclic tests (both CSSC and fatigue) were conducted three times for each sample series associated with both narrow and spread powders and post-operational treatments.

Vibration-induced fatigue tests were also carried out by using the shaker table shown in Figure 2 to analyse the influence of the powder particle size distribution under the HCF elastic fatigue behaviour

with shorter times than conventional tension/compression fatigue tests. Data acquisition was performed by HBM software. The tests were conducted using previously mentioned 120x20x2 mm samples of the third and fourth series. Each sample is clamped on one edge and held free on the other edge for vibration monitoring. No notches were applied to investigate the intrinsic influence of each parameter (powder characteristics, sample machining or heat-treatment) on the fatigue life. For these tests, we focused on the first bending resonance mode (pure bending) which provides a straightforward analytical relationship between sample deflection and stress. This first resonant frequency was tracked with a first SRTD (Sine Resonance Track and Dwell) [40–42] applied on the sample. An acceleration level of 1 g was used in a frequency range 50-120 Hz. All tests were performed with a sweep rate of 0.83Hz/s and duration of 1 minute. The resonance track was monitored by the frequency response corresponding to the output-input ratio. This frequency response was obtained respectively from a laser vibrometer (Polytec OFV 303) positioned at the free edge of samples and an accelerometer (PCB 333A30) bonded on the table to monitor and control the shaker.

A second SRTD was carried out then to perform the fatigue test at the previously characterized resonant frequency. The maximal stress values applied to the samples can be obtained using the sample deflection and bending stress formulas. In this case, to ensure elastic behaviour, maximal stress values in the range 200-250 MPa (about half the yield stress reported for 316L samples manufactured by LPBF [1,6,12,43]) were targeted. To this aim, the second test was performed with an acceleration of about 2g. Fracture was then detected by the drop of the resonance frequency. The controller automatically maintains the resonance conditions by tracking the resonant frequency during the test, even if a change causes a shift. Using this procedure, the frequency and time responses of all samples are continuously recorded during the fatigue tests.

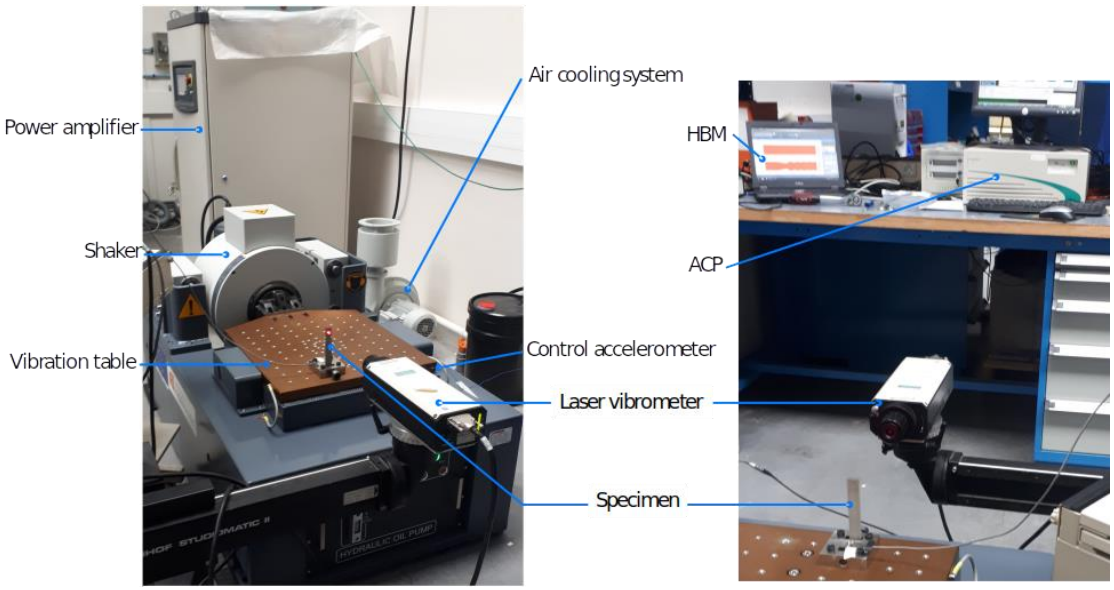

Figure 2: Illustration of the experimental set up for vibratory fatigue tests.

3. Results

3.1. Initial powder properties

The chemical compositions analysed by ICP-OES, GMDS and IGA are reported in Table 3. In particular, there are no significant differences in the Cr and Ni contents which may lead to variation in the stacking fault energy and further strain induced martensitic transformation ability. A difference in mechanical properties for samples manufactured from both powders cannot be due to the chemical composition.

Table 3: Powder chemical composition analyzed by ICP, GMDS and IGA (%weight).

Powder	Fe	C	Mn	Si	Cr	Ni	Cu	Mo	P	S	N	O
Narrow	Bal.	0.012	0.2	0.62	17.56	12.55	0.02	2.43	0.012	0.008	0.07	0.03
Spread	Bal.	0.015	0.19	0.58	17.51	12.56	0.02	2.44	0.012	0.008	0.07	0.02

The particle size distributions of these two powders, analysed by laser granulometry, are reported in Figure 3a in number fraction and in Figure 3b in volume fraction. The inset in Figure 3a exhibits the SEM illustrations of the powder particles. In number fraction, the spread powder has a larger number of particles with diameters larger than 20 µm. When plotted in volume fraction, the difference between the two powders is magnified with more than 50% of particles having diameters larger than 60 µm for the spread powder versus 15% for the narrow one. The spread of particle size is then much larger for the spread powder (particle size in the range 20-300 µm) than for the narrow one (particle size in the range 20-100 µm). The average powder particle size (d_{50}) is about 34 µm for the narrow powder versus 50 µm for the spread one. The two powders differ then by both average particle size and particle size distribution.

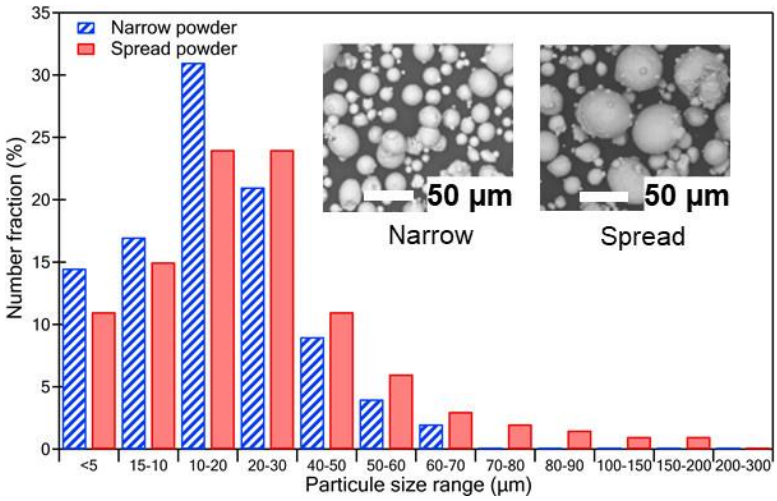

(a)

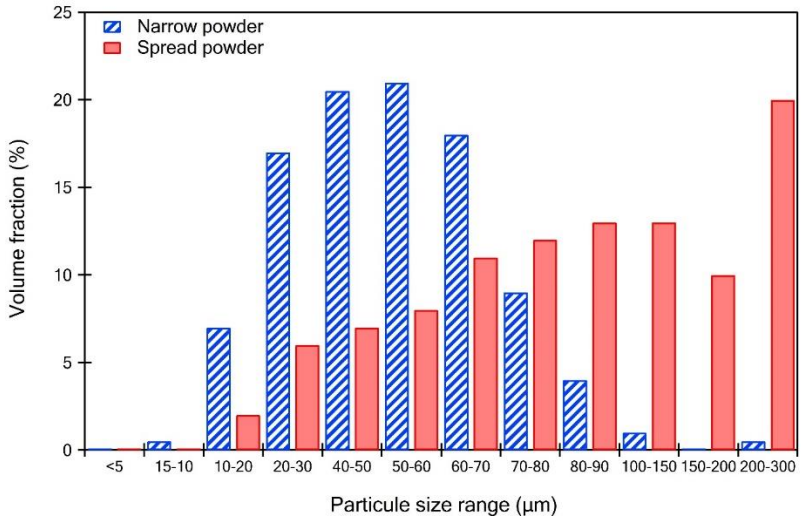

(b)

Figure 3: Particle size distribution of the narrow and spread powders employed for manufacturing: (a) number fraction distribution and (b) volume fraction distribution. Powders characteristics were analysed by laser granulometry.

Table 4 summarizes the powder characteristics, i.e. flowrate with Hall funnel, apparent and tap densities as well as avalanche energy, break energy, avalanche and rest angles. Except for the flowability measurement using the Hall funnel for which narrow powder did not flow, all other parameters are similar for the two kinds of powders.

Table 4: Summary of the powder flowability characteristics for the narrow and spread 316L powders.

Powder	Flowability (Hall Funnel) (s)	Tap density	Apparent density	Hausner ratio	Avalanche energy (mJ/kg)	Break energy (mJ/kg)	Avalanche angle (°)	Rest angle (°)
Narrow	n-a	4.77	4.50	1.06	17.55	43.16	44.23	33.00
Spread	15.58	4.81	4.35	1.10	17.48	41.48	45.20	32.23

3.2. Initial microstructure characterization

To investigate the influence of the powder particle size distribution and heat treatment on the microstructure of the built parts, density, surface roughness, dendrite and grain sizes and grain orientations were investigated.

3.2.1. Porosity, density and surface roughness analyses

LPBF process implies a different microstructure compared to cast or rolled samples with, in particular, defects such as pores or high surface roughness. Pores were observed for all samples and porosity was estimated by density measurements (Archimedes balance) and images analysis (together with the average pore size). Values are reported in Table 5.

All samples present a relative density of about 99% or higher which can be considered as highly dense samples. Similar result has been noticed in the literature irrespective of the scanning strategies [6,19,44,45]. The porosity measured by Archimedes methods is higher than the one measured by image analysis as already reported in the literature [36,46]. Results from image analysis show significant higher porosities for samples obtained from spread powder compared to narrow ones. The circularity and size of the pores are also affected by the powder particle distribution with an increase in the average pore size and decrease in circularity for spread powder. Indeed, more irregularly shaped pores are observed for spread powder. Moreover, the size of the manufactured samples (8 mm diameter for netshape series versus 20 mm for machined series) seems not to affect the porosity. When it comes to the effect of the heat treatment on porosity, considering both methods and their associated errors bars, no effect of this post-operational step is observed as already reported for such moderate temperature heat-treatments in literature [19,47,48].

Table 5: Porosity measurements by Archimedes and image analysis. Error bars are indicated for a confidence index of 90%.

	Porosity (%) (Archimedes)	Porosity (%) (Image analysis)	Circularity	Average pores surface (μm^2)
Netshape from spread powder (NS_S)	0.70 ± 0.10	0.11 ± 0.03	0.82 ± 0.03	89 ± 35
Machined from spread powder (M_S)	0.64 ± 0.22	0.06 ± 0.03	0.86 ± 0.03	76 ± 30
Machined from narrow powder (M_N)	0.66 ± 0.30	0.02 ± 0.02	0.98 ± 0.02	27 ± 15
Heat-treated from narrow powder (M_N_HT)	1.09 ± 0.13	0.01 ± 0.02	0.96 ± 0.02	10 ± 3
Heat-treated from spread powder (M_S_HT)	1.26 ± 0.68	0.09 ± 0.03	0.87 ± 0.03	71 ± 27

As already reported in literature, both average value and statistical distribution of the powder particles can affect the surface roughness [27,32]. For the narrow powder, the average of surface height deviation (Sa) is about 22.4 µm and 20.9 µm were measured for the 65° and 75° oriented walls, respectively. For the spread powder, slightly higher Sa values of about 25.7 and 22.8 µm was obtained for 65° and 75° oriented walls, in the order given. This increase in Sa characterized for samples manufactured from the spread powder is also associated to an increase in maximal peak/valley height difference with values of about 276 µm (65°) and 241 µm (75°) for those samples versus 251 µm (65°) and 217 µm (75°) for the ones built using the narrow powder.

3.2.2. Dendrites, grain size and texture analysis

SEM observations of sample cross-sections (not shown here) revealed that solidification mechanisms by dendrite nucleation and growth are observed for all manufacturing conditions. Precipitates are visible in melt pools boundaries and in the inter-dendritic space for all samples in agreement with previous studies [19,49]. A better insight of the initial dislocation structures for machined samples made from spread powder without heat-treatment is provided Figure 4a (M_S series) and Figure 4b with heat-treatment (M_S_HT series) by SEM-ECCI imaging. In this figure, it is clearly seen that the dendrite structure related to the manufacturing is affected by the heat-treatment. Indeed, for annealed samples, the dislocation cells show a loose character with a decrease in dislocation density in the inter-dendritic walls. Nevertheless, the average cell diameter is not modified by this moderate heat-treatment (both average values are about 0.41 µm), which thus only affects the dislocation density in the interdendritic space. For netshape sample, the average cell diameter is heterogeneous with a value of about 0.60 µm on a 1 mm layer below the free surface and a value of about 0.40 µm outside this layer.

Figure 5 shows the SEM-EBSD analysis (grain orientation maps and pole figures) of cross-sections perpendicular to the building direction for three conditions M_N, NS_S and M_S_HT series (see Table 2 for the sample identification). In the grain orientation maps, individual laser scan tracks are visible and are composed of small equiaxed grains and inter-track large grains for all samples including the heat-treated ones. A weak {110}<001> goss texture is observed on all pole figures in agreement with literature for a similar scanning strategy (67° rotation) [44]. However, the maximal pole density lower than five is supposed to ensure an isotropic mechanical behaviour for all samples.

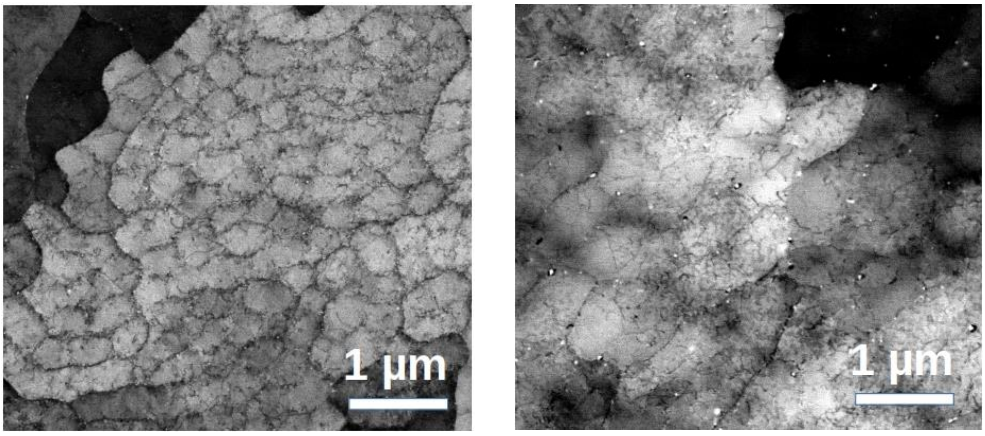

Figure 4: SEM-ECCI images of initial dislocations arrangements for the machined samples manufactured using spread powder: (a) without heat-treatment and (b) with heat-treatment (720°C- 2h).

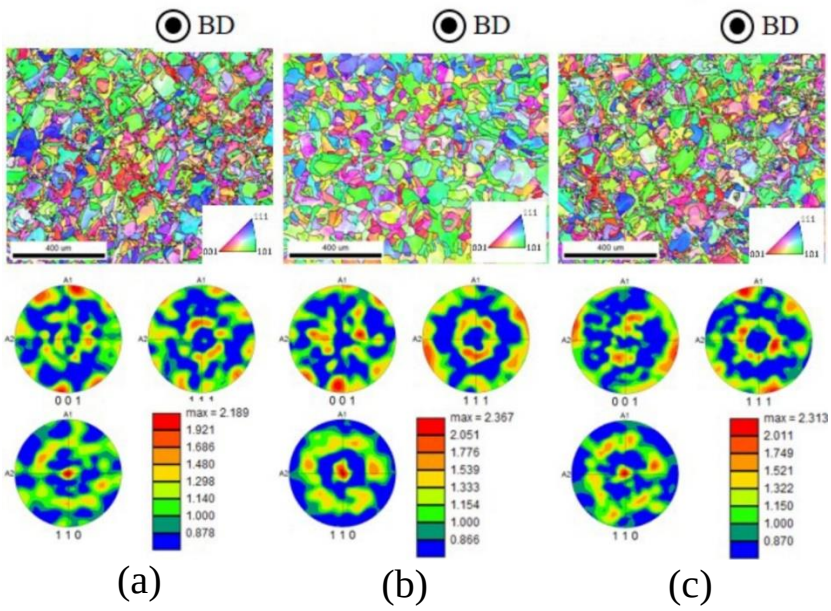

Figure 5: Grain orientation maps and associated pole figures for different samples: (a) machined specimen built with narrow powder (M_N), (b) netshape specimen built with spread powder (NS_S), and (c) heat-treated and machined specimen built with spread powder (M_S_HT).

Based on SEM-EBSD analysis reported in Figure 5, Table 6 summarizes the average grain size, aspect ratio, Grain Orientation Spread (GOS), Σ3 grain boundary fraction as well as low angle grain boundary fraction of the different samples. First, we can notice that these characteristics are independent of powder type and post-operational treatments. Average grain diameters are about 40 µm. Grain circularity is low (around 0.4) which cannot be explained by the presence of twin boundaries (almost no Σ3 grains boundaries). Indeed, most of the grain boundaries exhibit misorientations lower that 15°. Average grain orientation spread values exceed the 1° threshold generally associated to fully recrystallized and internal stress free materials [50]. All samples are then expected to exhibit internal residual stresses. Note that similar values of those parameters were estimated for other observation planes (not shown here) except for the aspect ratio due to the elongated grains related to epitaxial growth.

Table 6: Quantitative data obtained from the SEM-EBSD analysis: average grain diameter, grain shape aspect ratio (AR), average Grain Orientation Spread (GOS), proportion of Σ3 grains boundaries and proportion of low angle grain boundaries (GB<15°). Error bars are indicated for a confidence index of 90%.

	Diameter (µm)	AR	GOS (°)	Σ3	GB < 15°
Machined from narrow powder (M_N)	40 ± 25	0.40 ± 0.12	3.2 ± 1.9	0.34%	82%
Machined from spread powder (M_S)	37 ± 20	0.42 ± 0.14	3.1 ± 1.9	0.30%	82%
Netshape from spread powder (NS_S)	43 ± 20	0.40 ± 0.12	2.8 ± 1.4	0.50%	80%
Heat-treated from narrow powder (M_N_HT)	37 ± 22	0.42 ± 0.12	3.0 ± 1.5	0.35%	85%
Heat-treated from spread powder (M_S_HT)	38 ± 22	0.41 ± 0.12	2.8 ± 1.3	0.50%	82%

3.3. Mechanical properties

3.3.1. Monotonic tensile behaviour

First, samples were tested under monotonic tensile loading at room temperature to assess the conventional mechanical properties. The stress-strain curves depicted in Figure 6 show similar aspects for all considered samples. The average mechanical properties extracted from these curves are presented in Table 7. Results show that machining or powder characteristics do not influence tensile properties. In this work, except for the fracture strain which is slightly lower for the samples produced by spread powder, all other properties are similar. Heat treatment (720°C 2h) also enables a material softening with a decrease in the yield stress of about 80 MPa (15%), independently of the employed powder. When compared to literature, samples tested in this study present higher tensile strengths and higher ductility compared to cast samples [1,6,43] and even compared to other 316L manufactured by LPBF (yield stress: 380-600 MPa, UTS: 480-670 MPa, A %: 10-97%) [1,6,12,43].

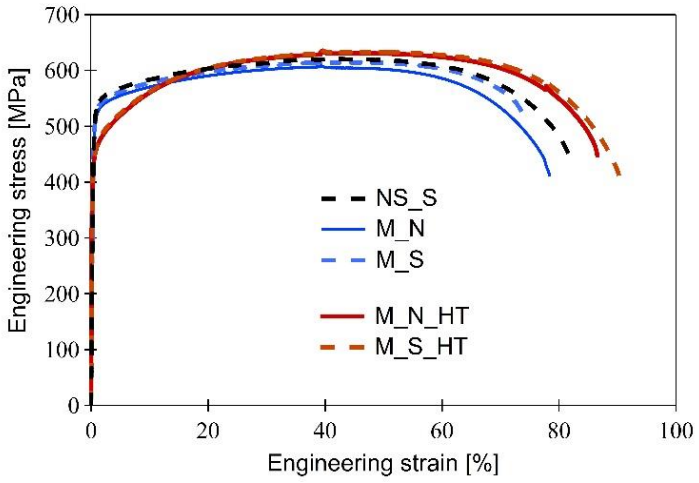

Figure 6: LPBF 316L engineering stress-strain curves obtained in tensile conditions for netshape (NS), machined (M) and heat-treated samples (_HT) manufactured from narrow (_N) and spread powder (_S).

Table 7: Summary of Ultimate Tensile Strength (UTS), 0.2% Yield Stress (YS), Homogeneous Maximal Elongation (HME) and elongation at fracture (A%) obtained in tensile tests for different powder particle distribution, machining and heat-treatment conditions. Error bars are indicated for a confidence index of 90%.

	YS [MPa]	UTS [MPa]	HME [%]	A [%]
Machined from narrow powder (M_N)	494 ± 9	618 ± 7	42 ± 2	86 ± 1
Machined from spread powder (M_S)	497 ± 11	622 ± 3	39 ± 1	73 ± 12
Netshape from spread powder (NS_S)	490 ± 40	619 ± 3	41 ± 2	78 ± 5
Heat-treated and machine from narrow powder (M_N_HT)	416 ± 7	618 ± 14	42 ± 3	92 ± 1
Heat-treated and machine from spread powder (M_S_HT)	422 ± 7	621 ± 13	41 ± 2	82 ± 4

3.3.2. Cyclic Stress-Strain Curves

Prior to the fatigue behaviour investigation, Cyclic Stress-Strain Curves (CSSC) were acquired to characterize the relationship between stress and plastic strain amplitudes and further define the fatigue conditions. Considering that monotonous properties are similar between machined and netshape samples, those CSSC tests were only performed on machined samples. The evolution of the average stress amplitude versus the average plastic strain amplitude is plotted in Figure 7a for the machined samples with and without heat-treatment. Each point corresponds to the average values stabilised after 250 cycles at the total applied strain. These cyclic tests were carried out for a number of total strain amplitude increments ranging from 10^{-4} to 10^{-2}, which leads to a plastic strain amplitude from 10^{-6} to 7.5×10^{-3} as shown in Figure 7a.

Figure 7a shows no significant differences in CSSC depending on powder characteristics – narrow or spread – even after a heat treatment. For non-heat-treated samples, a high cyclic strain hardening is observed up to plastic strain amplitudes of about $7x10^{-4}$ after which cyclic strain hardening is drastically reduced. This evolution is similar to the one observed on casted 316L samples after tensile pre-strains (involving dislocation cells formation) while fully recrystallized virgin samples do not exhibit any cyclic strain hardening for plastic strain amplitude lower than $7x10^{-4}$ [51]. For low plastic strain amplitudes (microplasticity), the stress amplitude is, surprisingly, much larger for heat-treated samples (hardening effect), while for high plastic strain amplitude (generalized plasticity), slight lower stresses (softening) are measured for those 720°C-2h annealed samples, similarly to the tensile yield stress.

Important residual stresses into additive manufactured materials are generally observed [1,52]. Cyclic tests with increasing plastic strain amplitude can be employed to estimate the average residual stress values [31]. For machined samples, mean stress evolution with the plastic strain amplitude depending on the kind of powder and heat-treatment is depicted in Figure 7b. For non-heat-treated samples, a negative mean stress is observed indicating tensile residual stresses. The mean stress reaches then a minimum value for plastic strain amplitudes about 10^{-4} which is close to the onset of homogeneous plasticity (yield locus crossed). After heat treatment, the evolution of the average stress with plastic strain amplitude is similar to the one observed for non-heat-treated samples. Nevertheless, residual stresses appear to have been partially released as the average stress value is reduced by a factor of two compared to as-built samples.

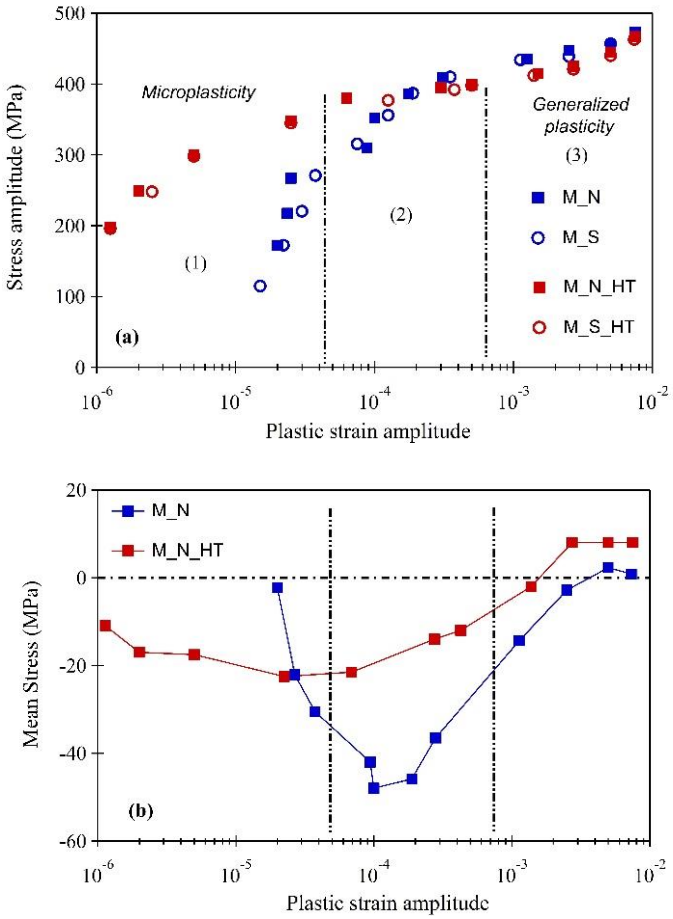

Figure 7: Average cyclic stress-strain curves of LPBF machined (M) samples obtained from narrow (_N) or spread (_S) powder without or with heat-treatment (_HT): (a) evolution of stress amplitude with plastic strain and (b) evolution of mean stress with plastic strain.

Based on these CSSC results, three plastic strain amplitudes (LCF, MCF and HCF) are chosen into domains 1, 2 and 3 (indicated in Figure 7a) to perform pure fatigue tests with a total strain amplitude control. Table 8 summarizes plastic strain and total strain amplitudes for the conducted fatigue tests. Due to the lower yield stress for heat-treated samples (see Table 7), total strain amplitude under HCF conditions was adapted for those samples to achieve similar plastic strain amplitude as non-heat-treated ones.

Table 8: Different strain amplitudes used for fatigue tests and associated plastic strain values.

	Low-cycle fatigue (LCF)	**Medium cycle fatigue (MCF)**	**High cycle fatigue (HCF)**
Plastic strain amplitude	$3x10^{-3}$	$5x10^{-4}$	$2x10^{-5}$
Total strain amplitude	$5x10^{-3}$	$2.5x10^{-3}$	$1.25x10^{-3}$ $1.75x10^{-3}$ (for H.T. samples)

3.3.3. Conventional fatigue behaviour

Figure 8 presents the fatigue behaviour for the three different total strain amplitudes considered in this work. First, Figure 8a shows the values of average plastic strain amplitudes of all the fatigue samples subjected to each fatigue conditions (i.e. LCF, MCF and HCF). For total strain amplitudes of about 5×10^{-3}, 2.5×10^{-3} and 1.25×10^{-3}, all samples exhibited similar average plastic strain amplitudes corresponding to about 3.10^{-3} (LCF), 5.10^{-4} (MCF) and 2.10^{-5} (HCF) respectively (as reported in Table 8). For each test series, it could be noted that those obtained plastic strain amplitudes correspond to that expected from the CSSC curves. Consequently, fatigue responses for netshape, machined and heat-treated samples made from each kind of powder can be easily compared for each applied total strain amplitudes. Then, Figure 8b, Figure 8c and Figure 8d, illustrate the evolution of the stress amplitude versus number of cycles for the LCF, MCF and HCF plastic strain amplitude, respectively. The increase in stress during the first tens of cycles corresponds to the cycles needed to reach the desired total strain amplitude.

As expected, the increase in the total strain amplitude results in an increase in the stress amplitude whereas the number of cycles to failure decreases. Moreover, when the applied plastic strain amplitude increases of one magnitude order, the number of cycles to failure decreases to one magnitude order. For the highest strain amplitude in fatigue (LCF - Figure 8b), no significant differences in stress amplitude appear between narrow and spread powders for both netshape and machined series. Nevertheless, for lower strain amplitudes, a slight decrease in fatigue life is observed in Figure 8c (MCF) and in Figure 8d (HCF) for the spread powder whereas stress amplitude is unchanged in agreement with the CSSC curves (see Figure 7a). Contrarily to the tensile tests for which no differences in mechanical properties between netshape and machined samples was observed (see Figure 6), in LCF and MCF conditions, netshape samples also exhibit a slightly reduced stress amplitude (between 10 and 20 MPa) compared to machined ones.

The effect of heat-treatment can be observed for each plastic strain amplitude. As predicted by CSSC curves, a softening effect is observed on heat-treated samples subjected to generalized plasticity (LCF and MCF conditions, see Figure 8b and Figure 8c, respectively) whereas a hardening is observed under the HCF conditions (Figure 10d). The softening of the stress amplitude is about 10 MPa and 20 MPa for the 3.10^{-3} and 5.10^{-4} plastic strain amplitudes respectively.

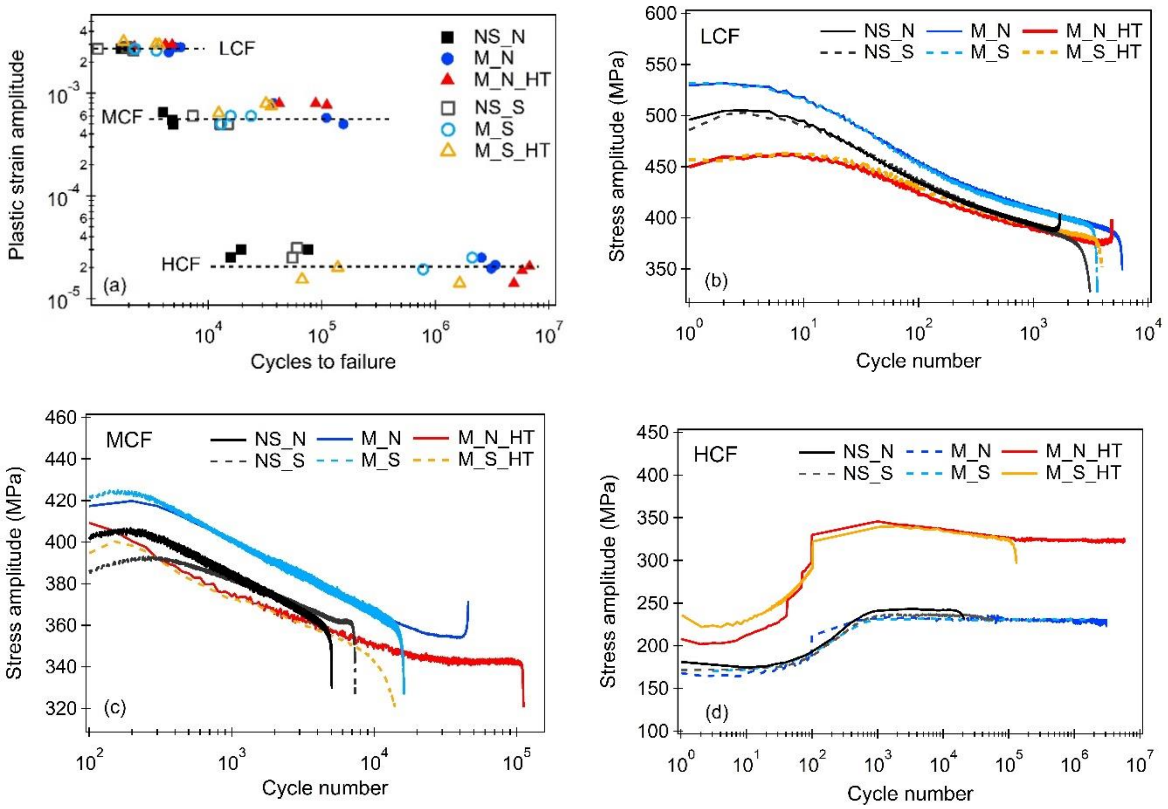

Figure 8: Fatigue behaviour for netshape (NS), machined (M) and heat-treated samples (_HT) manufactured from narrow (_N) and spread powder (_S): (a) average plastic strain amplitude versus number of cycles to failure, (b) fatigue curves 3×10^{-3} - LCF, (c) fatigue curves for $\Delta\varepsilon_p/2 = 5\times10^{-4}$ – MCF and, (d) fatigue curves for $\Delta\varepsilon_p/2 = 2\times10^{-5}$ – HCF.

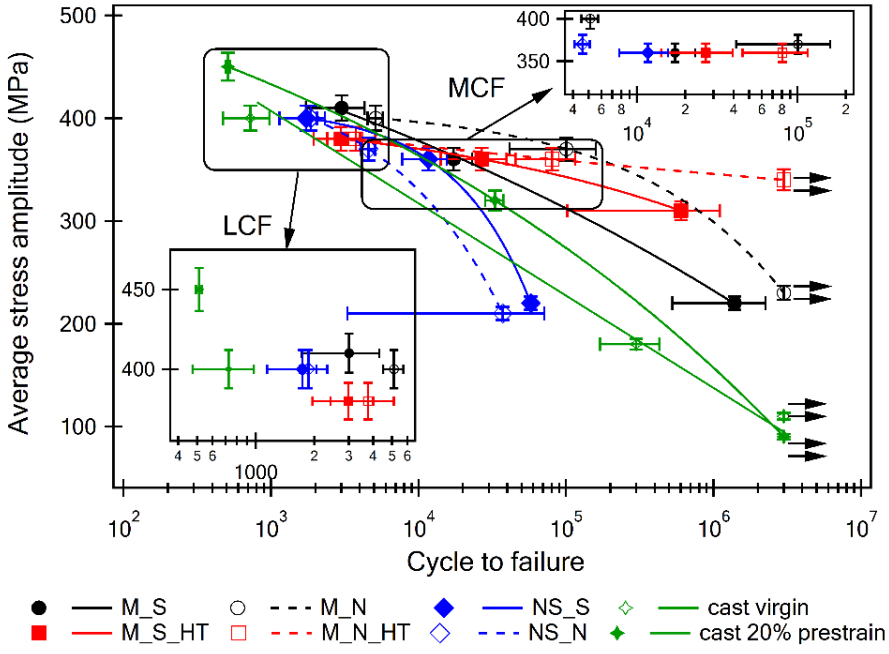

Figure 9: SN curves for netshape (NS), machined (M) and heat-treated samples (_HT) manufactured from narrow (_N) and spread powder (_S). For comparison purposes, cast virgin and cast 20% prestrained samples are introduced [53,54].

Finally, the evolution of the average stress amplitude versus the average cycle to failure (S-N curve) is plotted in Figure 9. Error bars (confidence index 90%) associated to the experimental scattering are introduced for each sample series. Two insets for LCF and MCF are introduced in this figure to better highlight the differences in fatigue behaviour between all samples. Compared to the machined specimens manufactured from the spread powder, a significant increase in fatigue life is observed for machined samples manufactured from narrow powder under both MCF and HCF conditions. In contrast to the machined samples, netshape ones present very low fatigue life. Regarding the influence of the stress relief heat treatment, no changes in fatigue lives is observed for the two highest plastic strain amplitudes when generalized plasticity is involved (LCF and MCF). For the lowest plastic strain amplitude, the heat-treatment improves the fatigue strength of the 316L samples manufactured by LPBF, independently of the kind of powder.

Literature data corresponding to conventional casted samples with different initial microstructures (fully recrystallized or tensile pre-strained) tested with similar plastic strain amplitudes [53,54] are compared to AM samples in Figure 9. In LCF conditions, compared to cast samples, AM ones exhibit similar average stress amplitude but significant increase in fatigue lives (about a factor of 3), including netshape samples. Under HCF, except netshape AM samples, all samples (AM and cast) did not break after one million cycles. Nevertheless, as for MCF, the average stress amplitude under HCF for AM series is larger than casted ones, in particular for the heat-treated ones for which this parameter is increased by a factor of 3.

3.3.4. Fatigue induced by vibration

The fatigue tests reported in the previous subsection were conducted in plasticity or microplasticity. However, in service, mechanical components are generally submitted to elastic HCF loadings. In order to investigate the effect of machining, powder characteristics and heat-treatment were conducted in vibration based-bending fatigue tests. The time signal recorded during the fatigue tests were used to extract the resonant frequency of each sample over the time. Since bending vibration tests generally do not lead to complete fracture after fatigue tests, the frequency drop must be used to define a failure criterion. This criterion was defined based on the Resonant Frequency Deviation (RFD). In the literature, the RFD was already used to correlate crack growth with the reduction in the resonant frequency due to crack initiation and propagation [55–59]. In these articles, the RFC threshold ranges between 0.5% and 5 % [55–59] for different metallic alloys. Here, for a confident failure detection, we chose to stop the tests at 5% below the initial resonant frequency to define the cycles to failure denoted $N_f^{5\%}$.

The evolutions of RFD as a function of applied cycles are depicted in Figure 10 for one sample of each sample series. Figure 10a illustrates the effect of the post-operational treatments (machining or annealing) for samples manufactured from the narrow powder, whereas Figure 10b denotes the effect of powder characteristics for the machined samples. In all cases, the resonant frequency remains unchanged during the first fatigue cycles, until the crack size reaches a critical value leading to a change in the resonant frequency. This change occurs for lower cycle number for the netshape samples compared to the machined one (Figure 10a), whereas the powder characteristics do not seem to strongly influence the fracture for that specific fatigue test (Figure 10b).

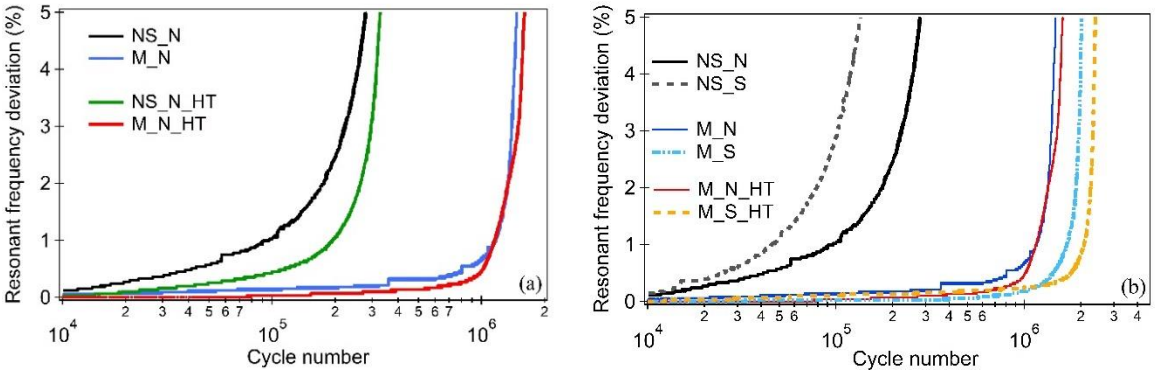

Figure 10: Evolution of the resonant frequency deviation during the bending fatigue tests for netshape (NS), machined (M) and heat-treated samples (_HT) manufactured from narrow (_N) and spread powder (_S): (a) effect of the machining and heat treatment on samples from narrow powder and (b) effect of the powder size particles (narrow vs spread powder).

The average cycles to failure $N_f^{5\%}$, their associated statistical scattering (confidence index 90%) and the average maximal stress values are reported in Table 9 for all samples tested in vibration. As for conventional fatigue tests, for comparison purposes, data of three casted samples with the same dimensions (labelled "CT") from commercial cold rolled plate, were added in this Table. These samples were also subjected to the same 720°C-2h heat-treatment.

For all AM sample series, Table 9 reports similar average maximal stress (located on the sample surface) of about 250 MPa whereas this value is about 200 MPa for cast samples. This value is similar to the stress amplitude associated to HCF conventional fatigue tests. No plastic deformation is then expected for this vibratory fatigue tests. Taking into account experimental scattering, the netshape samples exhibit cycles to failure reduced by a factor of 5 compared to machined ones as already observed for conventional fatigue tests. For this type of samples, contrarily to conventional fatigue tests, spread powder appears to be slightly detrimental to the fatigue life compared to narrow powder. Bending seems hence to magnify the effect of the weak difference in surface roughness between narrow and spread powders (see section 3.2) under the HCF fatigue life. For machined samples, considering the experimental scattering on the number of cycles to failure, powder characteristics do not seem to influence this parameter.

As for conventional fatigue tests, the 730-2h heat-treatment is beneficial for the cycles to failure independently on the sample series. Indeed, despite slightly larger average maximal stresses for the heat-treated samples, the number of cycles to failure is increased by about 100%. No significant fatigue life difference is observed between cast samples and machined AM samples independently on the precursor powder or heat-treatment sequence.

Table 9: Effect of machining, distribution of powder particle size and heat treatment on the fatigue lives ($N_f^{5\%}$) after bending fatigue in high cycle regime. Error bars are indicated for a confidence index of 90%.

Without heat treatment			With heat treatment		
Id	Average max. stress (MPa)	$N_f^{5\%}$ ($\times 10^6$)	Id	Average max. stress (MPa)	$N_f^{5\%}$ ($\times 10^6$)
CT	199 ± 11	2.45 ± 0.6	CT_HT	250 ± 22	3.35 ± 0.8
NS_V_N	243 ± 21	0.29 ± 0.06	NS_V_N_HT	277 ± 28	0.39 ± 0.06
NS_V_S	239 ± 21	0.16 ± 0.04	NS_V_S_HT	298 ± 60	0.43 ± 0.03
M_V_N	241 ± 16	1.43 ± 0.4	M_V_N_HT	284 ± 61	2.68 ± 0.3
M_V_S	238 ± 25	1.87 ± 0.7	M_V_S_HT	261 ± 30	3.78 ± 0.2

3.4. Microstructure investigation of HCF loaded samples

Previous experimental results show that under HCF, the average stress amplitude of AM samples is increased when subjected to stress relief heat treatments. In order to try to clarify this feature, TEM investigations were carried out after the fatigue tests to determine the changes in the microstructure, in particular on the dislocation arrangements. Figure 11 shows the Scanning Transmission Electron Microscopy (STEM) images of both machined and heat-treated samples subjected to HCF after 2 million cycles. Compared to the initial state (see Figure 6), the HCF did not induce any significant change in the dislocation structures, independently of the applied heat-treatment.

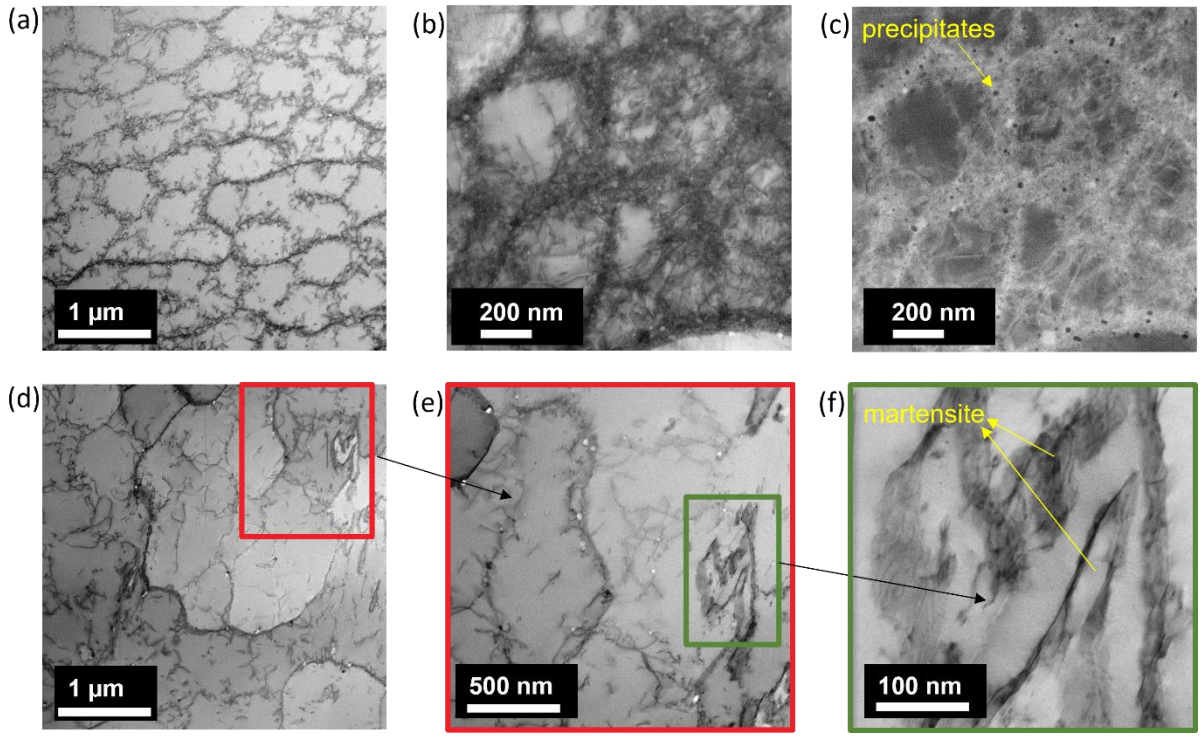

Figure 11: STEM images of dislocations arrangements after 2.10^6 cycles under HCF regime: (a, b, c) for machined samples without heat treatment; (d, e, f) for heat-treated samples. All pictures are related to bright field regime except c) which is taken with High Angle Annual Diffraction (HAADF) detector.

Many dislocations are visible in the dendrite walls as well as inside the dendrites (see Figure 11b). Precipitates are also observed in the interdendritic walls (Figure 11c) as a consequence of the high cooling rates representative of the laser powder bed fusion process [7]. Regarding the heat-treated samples, the loose character of dislocation cells is still observed in Figure 11d and Figure 11e. A lower dislocation density within the cells and in the cell walls compared to the non-annealed samples is also depicted. Moreover, Figure 11d, Figure 11e and Figure 11f also illustrate strain-induced α'-martensite clusters. This strain-induced α'-martensite formation is followed by a volume expansion that induces compressive stresses in the material, confirmed by the presence of the bending contours around the α'-martensite needle, due to the stress-relief during the thinning process of the TEM-foil [60].

Although the plastic strain amplitude during the fatigue test is similar for both samples (without and after heat treatment), TEM micrographs show that the formation of α'-martensite needles is more visible on the heat-treated samples. To validate these observations, a bulk measurement of the martensite content in the gauge section of samples was performed at the end of fatigue tests by means of a magneto-inductive testing using a feritscope. Figure 12 presents the results obtained for samples exposed to HCF regime. The heat-treated samples exhibit higher content of α'-martensite than the non-annealed machined samples. Without heat treatment, the magnetic fraction measurement is very low and does not exceed 0.05% (near to zero), which means that no austenite- α'-martensite transformation occurred. On the contrary, α'-martensite is detected on each zone of the gauge section of the heat-treated samples and the range is between 0.2% and 1.6%.

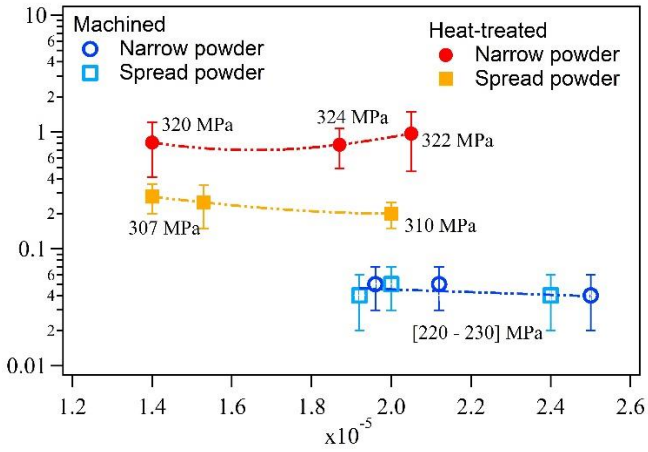

Figure 12: Magnetic fraction of α'-martensite measured by feritscope in the gauge section of samples after high cycle fatigue.

4. Discussion

The previous paragraphs highlighted the effect of a wide particle size distribution and the role played by machining or stress-relief heat treatments on the microstructure and mechanical properties, especially in fatigue. A slight decrease in fatigue life was observed for the spread powder compared to the narrow one which is not affected by post-operational treatments. The following paragraphs discuss these results in terms of powder flowability, sample porosity alongside with plastic strain.

4.1. Powder flowability, sample density and surface roughness.

The two powders employed in this investigation differ both in terms of average particle size or size distribution. The spread powder exhibits a larger d_{50} value (50 µm) compared to the narrow powder (34 µm) as well as a larger range of powder particle size, especially towards larger diameters. The results related to powder flowability summarized in Table 4 reports contradictory results. Indeed, the absence of powder flow of the narrow powder in the Hall funnel experience suggests that a narrow powder particle distribution could be detrimental to flowability. However, the Hausner ratio, defined as the ratio between tap and apparent density, is lower than 1.12 for the two powders (1.06 and 1.10 for the narrow and spread powder, respectively) which is qualified as excellent [61]. Therefore, based on those results, one could expect a worst powder particle spread on the powder bed for the narrow powder compared to the spread one, which must be detrimental to the density and further mechanical properties [62].

The increase in porosity observed in Table 5 clearly suggests an opposite trend with more uneven particle distribution in the powder bed for the spread powder. To better understand this discrepancy between powder flowability measurements and density/mechanical properties analysis, macroscopic observations of the powder bed after different passes of the recoater were realized on an experimental device simulating the powder bed during the LPBF process. To that aim, same recoater characteristics and same powder layer height (40 µm) were employed. The optical images related to the powder deposition are illustrated in Figure 13 for the two employed powders. Figure 13a and Figure 13b depict the deposition of the first layer on the plate for the narrow and spread powder, respectively. The particle distribution is very heterogeneous for this first powder layer with a more uneven powder particle distribution for the spread powder. This difference between the two powders in terms of powder bed quality is reduced when a second powder layer in deposited (no melting) as observed in Figure 13c – narrow powder and Figure 13d – spread powder. In that case, reduced areas exhibit lines linked to powder – recoater interactions. Nevertheless, in that case, the spread powder still exhibits the worst distribution in the plate with larger areas with low particle density. After three deposited layers, no macroscopic differences appear between the two powders with very similar homogeneous deposition as observed in Figure 13e and Figure 13f for the narrow and spread powders, in the order given.

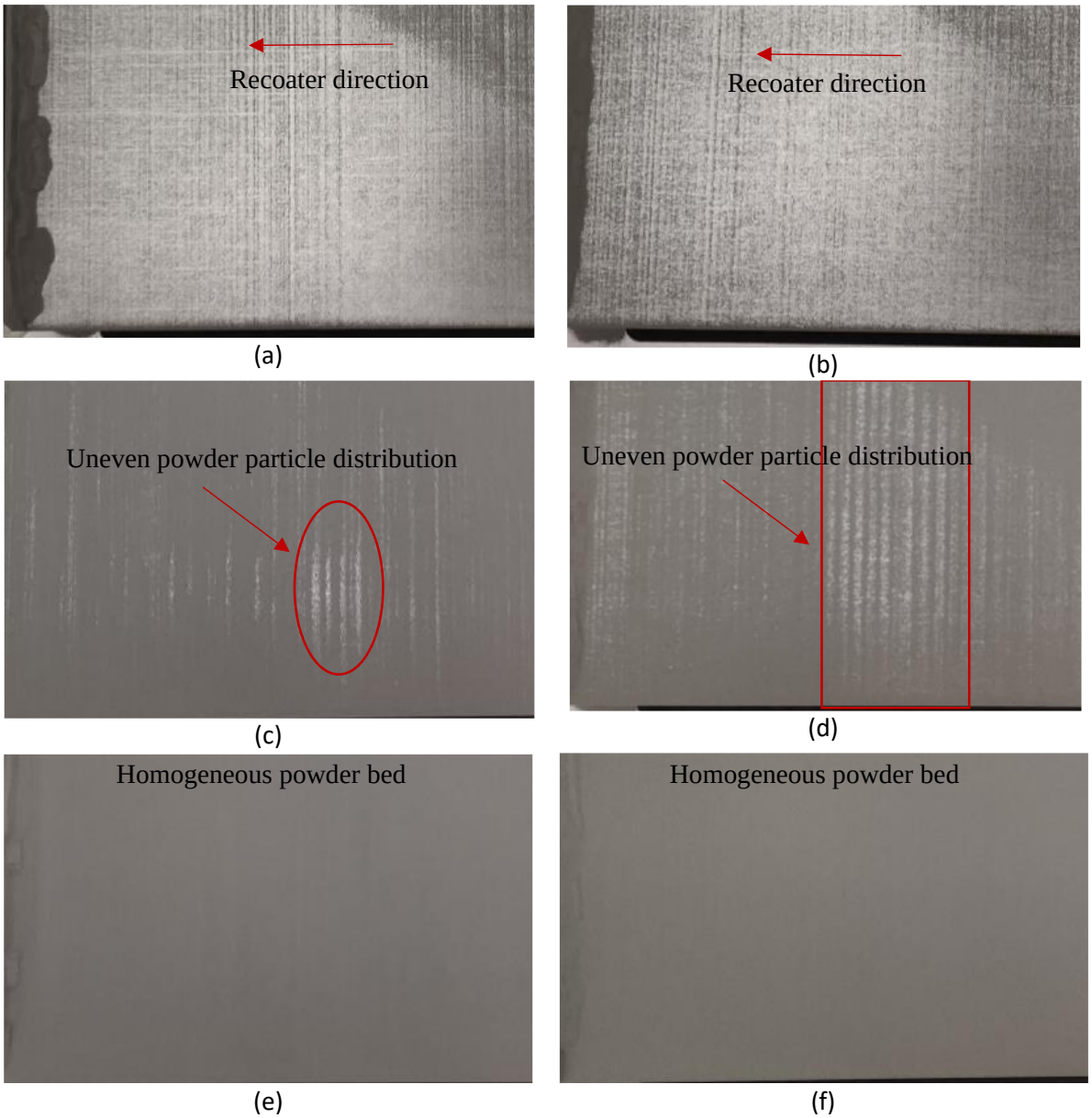

Figure 13*:* Illustration of the powder bed: after one powder layer deposition (a) narrow powder and (b) spread powder; after two layers deposition (c) narrow powder and (d) spread powder and after three layers deposition (e) narrow powder and (f) spread powder.

Despite the significant difference in powder characteristics, these observations illustrate a slightly worst particle distribution in the case of the spread powder compared to the narrow one, which nevertheless appears to be acceptable for AM based on the observations in Figure 13e and Figure 13f. Moreover, the extensive characterization of powder flowability performed in this study was not able to capture these differences. The relationship between the powder flowability measured in laboratory and the powder flow in the process still needs to be investigated.

According to the literature, the d_{50} value of a given powder out of the 28-38 µm range should be detrimental to density [34] whereas a wide spread of size could be beneficial to this parameter [35]. The results obtained in this study using a narrow and spread powder particle distribution seem to confirm Spurek and co-workers' assessment [34]. Indeed, despite a large spread of powder particles for the

spread powder, a slight decrease in density associated to pores with larger diameter and lower circularity was reported compared to the narrow powder (see Table 5). The similar grain size, dendrite size, GOS values for the samples manufactured from the two powders clearly shown that solidification mechanisms are not affected by the particle size distribution. The larger pore size for the spread powder cannot be due to a change from convection mode to a keyhole one which results in larger pores dimensions [1]. The slightly lower density for the spread powder is then due to the more uneven particle distribution of the powder involving lacks of fusion compared to the narrow one as discussed in the previous paragraph.

Regarding the surface roughness, results obtained in this study seem to indicate that the presence of particles having diameter up to 300 µm in the case of the spread powder leads to a higher surface roughness, whereas opposite results can be expected from the literature [35]. To conclude, a wide particle size distribution leads, hence, to a slightly larger porosity and surface roughness.

4.2. Effect of powder particle distribution and post-operational treatment on tensile behaviour.

In tension, the flow stress is not affected by the powder characteristics as grain size and dendrite size, expected to be the more influent parameters on the flow stress [63,64], are identical for samples produced from the two powders. According to literature, larger powder particles were found to enhance ductility [32,35,62]. Nevertheless, in the case of this study, the lower density and the presence of large pores for the spread powder reduce the fracture strain for the samples manufactured from this powder. This trend is confirmed by the observations of the fracture surfaces of the samples tested in tension. Figure 14a illustrates such a surface for a sample manufactured from the narrow powder, whereas Figure 14b depicts the fracture surface for a spread powder-based sample. For both specimens, the fracture surface highlights the pores, as illustrated in that figure. Nevertheless, the sample manufactured from the spread powder exhibits a larger density of pores associated to larger diameters compared to the narrow powder one. Moreover, for the spread powder, many of these pores exhibit unmelted powder particles (see Figure 14b inset) due to the lack of fusion. The slight increase in porosity rate characterized in Table 4 for the spread powder compared to the narrow one is then confirmed and magnified by this fracture surface characterization.

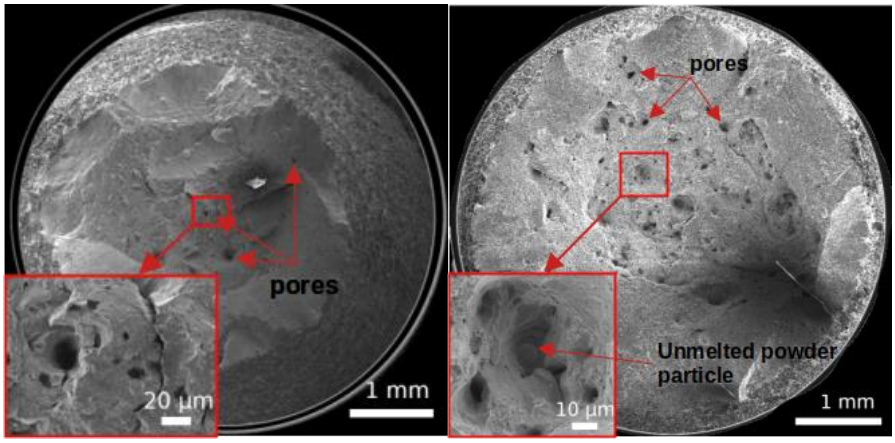

(a) (b)

Figure 14: SEM illustration of the fracture surfaces in tension for netshape sample manufactured from: (a) narrow powder and (b) spread powder.

When it comes to the effect of the machined/netshape sample character, netshape specimens shown an increase in the dislocation cell diameter in the vicinity of the surface (1 mm depth). Considering the link between dendrite (cell) size and cooling rate [65], this larger value on the surface must result from a lower cooling rate due to the contact with unmelted powder particles and/or to the contour fill. Nevertheless, as this change in microstructure is restricted on the subsurface only, no change in mechanical properties is characterized in tension. Besides, tensile conditions also induce a strain hardening which can quickly reduce the mechanical behaviour difference between the sample surface and the core areas. Finally, as observed in Figure 4, the stress-relief heat treatment (2h at 720°C) induces a decrease in dislocation density on the cell walls which, in turn, reduces the yield stress in agreement with reported results on hardness [48] and UTS [19] for the same material. This heat-treatment also induces a slight increase in strain to failure independently of the employed powder, probably due to the reduction in residual stresses suggested by both the slight decrease in GOS (Table 6) as well as the reduction in the average stress for cyclic loadings for the heat-treated samples (see Figure 7b).

4.3. Effect of powder particle distribution and post-operational treatment on cyclic and fatigue behaviour.

Under low cycle fatigue, despite the experimental scattering on the number of cycles to failure, results revealed that the wide range of particle size of the spread powder, associated to the larger porosity rate, tends to slightly reduce the fatigue life compared to the narrow powder. This feature is in agreement with the established results regarding fatigue and metallurgical defects [66–68]. This fatigue life is, moreover, not affected by the stress relief heat treatment, whereas the large surface roughness for the netshape samples also decreases the fatigue life. Nevertheless, for LCF, those variation in fatigue lives are rather small and all values of cycles to failure are of the same order of magnitude. Despite their machined character, the cast samples, including those previously deformed in tension and exhibiting well-formed dislocation cells [53], have fatigue lives of an order of magnitude lower than AM ones (see Figure 9). The microstructure of AM manufacturing samples and especially the very stable dislocation cells inherited from the solidification process [69] seem to reduce the plastic damage related to the high plastic strain amplitude related to LCF.

For lower plastic strain amplitude (MCF conditions), the difference in fatigue life between all samples is increased. In that case, for the machined samples, the reduction in the number of cycles to failure is reduced by 80% when powder is changed from narrow to spread. This trend is not affected by the heat-treatment whereas the netshape character, surprisingly, seems to be more detrimental to fatigue life when narrow powder is employed despite a higher surface roughness. As for LCF conditions, the netshape character also induces a reduction in stress amplitude of about 30 MPa compared to the machined samples. This softening could be due to the larger dislocation cell diameter in the vicinity of the surface which is not observed in tension due to the strain hardening occurring since the beginning of plasticity. Compared to the cast samples (virgin or tensile deformed), for the same plastic strain amplitude, the AM samples exhibit larger stress amplitudes. For the tensile deformed cast samples, the average cycles to failure ranges are between those of the machined samples. Under MCF conditions, the average stress amplitude for the virgin cast sample is about half the one of the AM for a cycle-to-failure value in the same order of magnitude as the M_N samples. This is because under MCF condition, fatigue damage is more dependent on surface defects such as surface roughness. In that case, the machined AM and cast samples behave similarly. Nevertheless, as under LCF conditions, the

higher stress amplitude clearly illustrates the superiority of the AM samples compared to the cast samples.

Under HCF conditions, strong differences in fatigue behaviour are observed. At such low plastic strain amplitudes, the surface defects are dominant over the fracture initiation [70]. As a result, netshape samples exhibit a lower number of cycles to failure by more than one order of magnitude compared to machined samples, which in some cases did not break after 3 million cycles (in agreement with the literature [55,57,58]). For these machined samples, the powder particle distribution effect is similar to the one observed under MCF conditions with a decrease in the average number of cycles to failure for samples built with spread powder. In that specific fatigue loading conditions, the heat treatment at 720°C during 2h increases of about 100-150 MPa the average stress amplitude for similar fatigue lives. This result seems to be in agreement with the increase in the endurance limit from 310 to 360 MPa reported by Blinn et al. [15] for 316L samples manufactured by LPBF and further subjected to a heat treatment at 650°C during 2h. Nevertheless, this stress amplitude increase is opposite to the softening observed in tension, LCF and MCF conditions but is consistent with the hardening observed in CSSC curves. This feature suggests a microstructural change after the heat-treatment as the modification in residual stress (characterized in Figure 7b) and reported in the literature [52] would imply the same softening or hardening, independently of the applied total strain amplitude.

The vibration fatigue confirmed these results obtained under HCF tests and provided additional information. Indeed, the heat-treatment performed on the different samples increases both average stress amplitude but also the fatigue lives for all AM samples (results on cast are not significantly different). Recent work on residual stresses [52] for AM samples proved that the tensile residual stress in the free surface vicinity is decreased when stress relief heat treatments are applied. This, in turn, can reduce the fatigue damage on the surface, as observed here, independently of the kind of samples.

4.4. Effect of heat treatment on martensitic transformation.

The martensitic phase transformation occurring in HCF conditions for heat-treated samples could explain the increase in stress amplitude compared to the non-heat-treated samples. Following Grigorescu *et al.* [60], who observed a significant amount of martensite content after very high cycle fatigue in a 316L steel previously annealed at 1050°C, the activation of multiple slip systems enhances the formation of the α'-martensite. This martensitic phase then improves the fatigue behaviour by reducing crack initiation due to the local compressive residual stresses. For AM 316L, it has shown that the martensitic phase transformation occurs preferentially on the dendrite walls due to the larger concentration of Cr and Mo with respect to the matrix [71]. In our case, the decrease in dislocation density in the dendrite walls for heat-treated samples could promote multiple slip in those areas inducing a larger tendency to phase transformation which can also be enhanced by Cr diffusion on the dislocation walls during heat-treatment. This increase in α'-martensite may lead, in turn, to an improvement in stress amplitude and fatigue life. However, as the amount of martensitic phase is below 2% for heat-treated samples, this mechanism, alone, cannot be responsible for the stress amplitude increment for heat-treated samples subjected to HCF or vibration fatigue. Other mechanisms (short-range order, nano-scale precipitation, Cottrel atmospheres, etc) could also promote the improved fatigue behaviour for heat-treated samples. Work is in progress to better clarify this point and the origin of the difference in martensite content after HCF between narrow and spread powders with similar Cr and Ni content (see Table 3).

5. Conclusions

In this study, the effect of particle size distribution (narrow and widely spread) on the microstructure and the mechanical properties of a stainless steel AISI 316L produced by laser powder bed fusion was investigated. Different post-operational conditions (machining with or without stress relief heat-treatment) were considered. By an extensive characterization of the precursor powder characteristics combined to the microstructure, the tension and fatigue properties (from LCF to HCF and vibration fatigue) of the printed parts, the following conclusions can be drawn:

- A large spread of particle diameters is slightly detrimental to flowability which is not captured by any conventional powder flowability parameter.

- A slight increase in porosity is observed when a large spread of particle sizes is employed due to a more uneven distribution of powder in the plate. Phases, grain size, texture and dendrite sizes are not affected by the powder particle distribution and are independent of the post-operational heat-treatments.

- Tensile properties are unaffected by powder characteristics or machining, whereas a 2h heat-treatment at 720°C induces a 15% decrease in yield stress due to a reduction in initial dislocation density.

- In fatigue, for the machined samples, the powder characteristics influence the fatigue life under HCF conditions with a weak detrimental character of spread powder associated with a slightly larger porosity.

- The applied heat-treatment of 720°C for 2h significantly increases the fatigue behaviour under HCF conditions with an increase in the stress amplitude (for a given applied plastic strain amplitude) and the number of cycles to failure. This effect could be due to a larger ability of α'-martensite transformation and a decrease in tensile residual stresses at the sample surface.

Those results clearly suggest that the influence of a very large powder particle distribution is, in all cases, lower that the one related to the surface roughness (netshape versus machined character) and heat-treatment. Moreover, compared to conventional machined cast samples, AM samples exhibit better tensile and fatigue behaviour independently of the employed powder. Powders with a very large particle size distribution, resulting for instance from a mixed powder batch, could be acceptable for additive manufacturing using powder bed processes.

Acknowledgments

Yan Duval is acknowledged for the help on the fatigue data treatment. Sebastien Vernay from Normandy Aerospace is also acknowledged for the administrative support on the CLIP FAM project.

Funding

The Normandy Region and European Union (European Regional Development Fund) are greatly acknowledged for the financial support of the CLIP FAM project.

Conflict of interest/Competing interest

The authors declare no competing interest

Availability of data and materials

The raw/processed data required to reproduce these findings cannot be shared as the data also forms part of an ongoing study.

Code availability

Not applicable

Ethics approval

Not applicable

Consent to participate

Not applicable

Consent to publication

Not applicable

Authors' contribution

J. Ngeijio: conceptualization, investigation, writing and editing. **M. Mokhari**: conceptualization, investigation, writing and editing, **E. Paccou**: investigation. **E. Bauster**: conceptualization. **L. Khalij**: investigation, writing and editing. **E. Hug**: conceptualization, writing and editing. **P. Bernard**: conceptualization. **S. Boileau**: conceptualization, investigation. **C. Keller**: project supervision, conceptualization, investigation, writing and editing.

References

[1] T. DebRoy, H.L. Wei, J.S. Zuback, T. Mukherjee, J.W. Elmer, J.O. Milewski, A.M. Beese, A. Wilson-Heid, A. De, W. Zhang, Additive manufacturing of metallic components – Process, structure and properties, Progress in Materials Science. 92 (2018) 112–224. https://doi.org/10.1016/j.pmatsci.2017.10.001.

[2] C. Zhao, K. Fezzaa, R.W. Cunningham, H. Wen, F. De Carlo, L. Chen, A.D. Rollett, T. Sun, Real-time monitoring of laser powder bed fusion process using high-speed X-ray imaging and diffraction, Sci Rep. 7 (2017) 3602. https://doi.org/10.1038/s41598-017-03761-2.

[3] A. Leicht, U. Klement, E. Hryha, Effect of build geometry on the microstructural development of 316L parts produced by additive manufacturing, Materials Characterization. 143 (2018) 137–143. https://doi.org/10.1016/j.matchar.2018.04.040.

[4] F. Yan, W. Xiong, E. Faierson, G.B. Olson, Characterization of nano-scale oxides in austenitic stainless steel processed by powder bed fusion, Scripta Materialia. 155 (2018) 104–108. https://doi.org/10.1016/j.scriptamat.2018.06.011.

[5] Z. Sun, X. Tan, S.B. Tor, C.K. Chua, Simultaneously enhanced strength and ductility for 3D-printed stainless steel 316L by selective laser melting, NPG Asia Mater. 10 (2018) 127–136. https://doi.org/10.1038/s41427-018-0018-5.

[6] X. Wang, J.A. Muñiz-Lerma, O. Sánchez-Mata, M. Attarian Shandiz, M. Brochu, Microstructure and mechanical properties of stainless steel 316L vertical struts manufactured by laser powder bed fusion process, Materials Science and Engineering: A. 736 (2018) 27–40. https://doi.org/10.1016/j.msea.2018.08.069.

[7] A. Ahmadi, R. Mirzaeifar, N.S. Moghaddam, A.S. Turabi, H.E. Karaca, M. Elahinia, Effect of manufacturing parameters on mechanical properties of 316L stainless steel parts fabricated by selective laser melting: A computational framework, Materials & Design. 112 (2016) 328–338. https://doi.org/10.1016/j.matdes.2016.09.043.

[8] W.M. Tucho, V.H. Lysne, H. Austbø, A. Sjolyst-Kverneland, V. Hansen, Investigation of effects of process parameters on microstructure and hardness of SLM manufactured SS316L, Journal of Alloys and Compounds. 740 (2018) 910–925. https://doi.org/10.1016/j.jallcom.2018.01.098.

[9] D. Gu, Y. Shen, Processing conditions and microstructural features of porous 316L stainless steel components by DMLS, Applied Surface Science. 255 (2008) 1880–1887. https://doi.org/10.1016/j.apsusc.2008.06.118.

[10] E. Liverani, S. Toschi, L. Ceschini, A. Fortunato, Effect of selective laser melting (SLM) process parameters on microstructure and mechanical properties of 316L austenitic stainless steel, Journal of Materials Processing Technology. 249 (2017) 255–263. https://doi.org/10.1016/j.jmatprotec.2017.05.042.

[11] R. Shrestha, J. Simsiriwong, N. Shamsaei, Fatigue behavior of additive manufactured 316L stainless steel parts: Effects of layer orientation and surface roughness, Additive Manufacturing. 28 (2019) 23–38. https://doi.org/10.1016/j.addma.2019.04.011.

[12] T. Kurzynowski, K. Gruber, W. Stopyra, B. Kuźnicka, E. Chlebus, Correlation between process parameters, microstructure and properties of 316 L stainless steel processed by selective laser melting, Materials Science and Engineering: A. 718 (2018) 64–73. https://doi.org/10.1016/j.msea.2018.01.103.

[13] S. Afkhami, M. Dabiri, S.H. Alavi, T. Björk, A. Salminen, Fatigue characteristics of steels manufactured by selective laser melting, International Journal of Fatigue. 122 (2019) 72–83. https://doi.org/10.1016/j.ijfatigue.2018.12.029.

[14] C. Elangeswaran, A. Cutolo, G.K. Muralidharan, C. de Formanoir, F. Berto, K. Vanmeensel, B. Van Hooreweder, Effect of post-treatments on the fatigue behaviour of 316L stainless steel manufactured by laser powder bed fusion, International Journal of Fatigue. 123 (2019) 31–39. https://doi.org/10.1016/j.ijfatigue.2019.01.013.

[15] B. Blinn, F. Krebs, M. Ley, R. Teutsch, T. Beck, Determination of the influence of a stress-relief heat treatment and additively manufactured surface on the fatigue behavior of selectively laser melted AISI 316L by using efficient short-time procedures, International Journal of Fatigue. 131 (2020) 105301. https://doi.org/10.1016/j.ijfatigue.2019.105301.

[16] X. Liang, C. Robert, A. Hor, F. Morel, Numerical investigation of the surface and microstructure effects on the high cycle fatigue performance of additive manufactured stainless steel 316L, International Journal of Fatigue. 149 (2021) 106273. https://doi.org/10.1016/j.ijfatigue.2021.106273.

[17] S. Afkhami, M. Dabiri, H. Piili, T. Björk, Effects of manufacturing parameters and mechanical post-processing on stainless steel 316L processed by laser powder bed fusion, Materials Science and Engineering: A. 802 (2021) 140660. https://doi.org/10.1016/j.msea.2020.140660.

[18] B. AL-Mangour, P. Vo, R. Mongrain, E. Irissou, S. Yue, Effect of Heat Treatment on the Microstructure and Mechanical Properties of Stainless Steel 316L Coatings Produced by Cold Spray for Biomedical Applications, J Therm Spray Tech. 23 (2014) 641–652. https://doi.org/10.1007/s11666-013-0053-2.

[19] T. Ronneberg, C.M. Davies, P.A. Hooper, Revealing relationships between porosity, microstructure and mechanical properties of laser powder bed fusion 316L stainless steel through heat treatment, Materials & Design. 189 (2020) 108481. https://doi.org/10.1016/j.matdes.2020.108481.

[20] H. Gu, H. Gong, J. j. s Dilip, D. Pal, A. Hicks, H. Doak, B. Stucker, Effects of Powder Variation on the Microstructure and Tensile Strength of Ti6Al4V Parts Fabricated by Selective Laser Melting, in: 2014.

[21] M. Thomas, T. De Terris, S. Drawin, Impact des caractéristiques des poudres sur les propriétés des matériaux métalliques élaborés par fabrication additive, Traitements et Matériaux. 447 (2017) 22–31.

[22] C. Pleass, S. Jothi, Influence of powder characteristics and additive manufacturing process parameters on the microstructure and mechanical behaviour of Inconel 625 fabricated by Selective Laser Melting, Additive Manufacturing. 24 (2018) 419–431. https://doi.org/10.1016/j.addma.2018.09.023.

[23] J. Slotwinski, E. Garboczi, P. Stutzman, C. Ferraris, S. Watson, M. Peltz, Characterization of Metal Powders Used for Additive Manufacturing, J Res Natl Inst Stand Technol. 119 (2014) 460–493. https://doi.org/10.6028/jres.119.018.

[24] L.C. Ardila, F. Garciandia, J.B. González-Díaz, P. Álvarez, A. Echeverria, M.M. Petite, R. Deffley, J. Ochoa, Effect of IN718 Recycled Powder Reuse on Properties of Parts Manufactured by Means of Selective Laser Melting, Physics Procedia. 56 (2014) 99–107. https://doi.org/10.1016/j.phpro.2014.08.152.

[25] D. Powell, A.E.W. Rennie, L. Geekie, N. Burns, Understanding powder degradation in metal additive manufacturing to allow the upcycling of recycled powders, Journal of Cleaner Production. 268 (2020) 122077. https://doi.org/10.1016/j.jclepro.2020.122077.

[26] M.J. Heiden, L.A. Deibler, J.M. Rodelas, J.R. Koepke, D.J. Tung, D.J. Saiz, B.H. Jared, Evolution of 316L stainless steel feedstock due to laser powder bed fusion process, Additive Manufacturing. 25 (2019) 84–103. https://doi.org/10.1016/j.addma.2018.10.019.

[27] P. Quinn, S. O'Halloran, J. Lawlor, R. Raghavendra, The effect of metal EOS 316L stainless steel additive manufacturing powder recycling on part characteristics and powder reusability, Advances in Materials and Processing Technologies. 5 (2019) 348–359. https://doi.org/10.1080/2374068X.2019.1594602.

[28] B.A. Hann, Powder Reuse and Its Effects on Laser Based Powder Fusion Additive Manufactured Alloy 718, SAE Int. J. Aerosp. 9 (2016) 209–213. https://doi.org/10.4271/2016-01-2071.

[29] O.A. Quintana, J. Alvarez, R. Mcmillan, W. Tong, C. Tomonto, Effects of Reusing Ti-6Al-4V Powder in a Selective Laser Melting Additive System Operated in an Industrial Setting, JOM. 70 (2018) 1863–1869. https://doi.org/10.1007/s11837-018-3011-0.

[30] H.P. Tang, M. Qian, N. Liu, X.Z. Zhang, G.Y. Yang, J. Wang, Effect of Powder Reuse Times on Additive Manufacturing of Ti-6Al-4V by Selective Electron Beam Melting, JOM. 67 (2015) 555–563. https://doi.org/10.1007/s11837-015-1300-4.

[31] E. Paccou, M. Mokhtari, C. Keller, J. Nguejio, W. Lefebvre, X. Sauvage, S. Boileau, P. Babillot, P. Bernard, E. Bauster, Investigations of powder reusing on microstructure and mechanical properties of Inconel 718 obtained by additive manufacturing, Materials Science and Engineering: A. 828 (2021) 142113. https://doi.org/10.1016/j.msea.2021.142113.

[32] B. Liu, R. Wildman, C. Tuck, I. Ashcroft, R. Hague, Investigaztion the effect of particle size distribution on processing parameters optimisation in selective laser melting process, 22nd Annual International Solid Freeform Fabrication Symposium - An Additive Manufacturing Conference, SFF 2011. (2011).

[33] R. Groarke, C. Danilenkoff, S. Karam, E. McCarthy, B. Michel, A. Mussatto, J. Sloane, A. O' Neill, R. Raghavendra, D. Brabazon, 316L Stainless Steel Powders for Additive Manufacturing: Relationships of Powder Rheology, Size, Size Distribution to Part Properties, Materials. 13 (2020) 5537. https://doi.org/10.3390/ma13235537.

[34] M.A. Spurek, L. Haferkamp, C. Weiss, A.B. Spierings, J.H. Schleifenbaum, K. Wegener, Influence of the particle size distribution of monomodal 316L powder on its flowability and processability in powder bed fusion, Prog Addit Manuf. 7 (2022) 533–542. https://doi.org/10.1007/s40964-021-00240-z.

[35] A.B. Spierings, N. Herres, G. Levy, Influence of the particle size distribution on surface quality and mechanical properties in AM steel parts, Rapid Prototyping Journal. 17 (2011) 195–202. https://doi.org/10.1108/13552541111124770.

[36] A.B. Spierings, M. Schneider, R. Eggenberger, Comparison of density measurement techniques for additive manufactured metallic parts, Rapid Prototyping Journal. 17 (2011) 380–386. https://doi.org/10.1108/13552541111156504.

[37] S. Ziri, A. Hor, C. Mabru, Combined effect of powder properties and process parameters on the density of 316L stainless steel obtained by laser powder bed fusion, Int J Adv Manuf Technol. 120 (2022) 6187–6204. https://doi.org/10.1007/s00170-022-09160-w.

[38] M. Yakout, M.A. Elbestawi, S.C. Veldhuis, On the characterization of stainless steel 316L parts produced by selective laser melting, Int J Adv Manuf Technol. 95 (2018) 1953–1974. https://doi.org/10.1007/s00170-017-1303-0.

[39] J. Schindelin, I. Arganda-Carreras, E. Frise, V. Kaynig, M. Longair, T. Pietzsch, S. Preibisch, C. Rueden, S. Saalfeld, B. Schmid, J.-Y. Tinevez, D.J. White, V. Hartenstein, K. Eliceiri, P. Tomancak, A. Cardona, Fiji: an open-source platform for biological-image analysis, Nat Methods. 9 (2012) 676–682. https://doi.org/10.1038/nmeth.2019.

[40] V. Rouillard, M.A. Sek, A frequency domain technique for maintaining resonance condition during sine dwell vibration testing of packages, Packaging Technology and Science. 13 (2000) 227–232. https://doi.org/10.1002/pts.520.

[41] Joel, Minderhoud, Improving SRTD Testing with Resonance Phase Settings, Sound & Vibration. 47 (2013) 12–14.

[42] Q. Su, J. Pitarresi, M. Gharaibeh, A. Stewart, G. Joshi, M. Anselm, Accelerated vibration reliability testing of electronic assemblies using sine dwell with resonance tracking, in: 2014 IEEE 64th Electronic Components and Technology Conference (ECTC), 2014: pp. 119–125. https://doi.org/10.1109/ECTC.2014.6897276.

[43] A. Röttger, K. Geenen, M. Windmann, F. Binner, W. Theisen, Comparison of microstructure and mechanical properties of 316L austenitic steel processed by selective laser melting with hot-isostatic pressed and cast material, Materials Science and Engineering: A. 678 (2016) 365–376. https://doi.org/10.1016/j.msea.2016.10.012.

[44] S. Bahl, S. Mishra, K.U. Yazar, I.R. Kola, K. Chatterjee, S. Suwas, Non-equilibrium microstructure, crystallographic texture and morphological texture synergistically result in unusual mechanical properties of 3D printed 316L stainless steel, Additive Manufacturing. 28 (2019) 65–77. https://doi.org/10.1016/j.addma.2019.04.016.

[45] U. Scipioni Bertoli, B.E. MacDonald, J.M. Schoenung, Stability of cellular microstructure in laser powder bed fusion of 316L stainless steel, Materials Science and Engineering: A. 739 (2019) 109–117. https://doi.org/10.1016/j.msea.2018.10.051.

[46] G. Puppala, A. Moitra, S. Sathyanarayanan, R. Kaul, G. Sasikala, R.C. Prasad, L.M. Kukreja, Evaluation of fracture toughness and impact toughness of laser rapid manufactured Inconel-625 structures and their co-relation, Materials & Design. 59 (2014) 509–515. https://doi.org/10.1016/j.matdes.2014.03.013.

[47] X. Yang, F. Tang, X. Hao, Z. Li, Oxide Evolution During the Solidification of 316L Stainless Steel from Additive Manufacturing Powders with Different Oxygen Contents, Metall Mater Trans B. 52 (2021) 2253–2262. https://doi.org/10.1007/s11663-021-02191-w.

[48] E. Tascioglu, Y. Karabulut, Y. Kaynak, Influence of heat treatment temperature on the microstructural, mechanical, and wear behavior of 316L stainless steel fabricated by laser powder bed additive manufacturing, Int J Adv Manuf Technol. 107 (2020) 1947–1956. https://doi.org/10.1007/s00170-020-04972-0.

[49] O.O. Salman, C. Gammer, A.K. Chaubey, J. Eckert, S. Scudino, Effect of heat treatment on microstructure and mechanical properties of 316L steel synthesized by selective laser melting, Materials Science and Engineering: A. 748 (2019) 205–212. https://doi.org/10.1016/j.msea.2019.01.110.

[50] K. Sitarama Raju, M. Ghanashyam Krishna, K.A. Padmanabhan, V. Subramanya Sarma, N.P. Gurao, G. Wilde, Microstructure evolution and hardness variation during annealing of equal channel angular pressed ultra-fine grained nickel subjected to 12 passes, J Mater Sci. 46 (2011) 2662–2671. https://doi.org/10.1007/s10853-010-5122-z.

[51] G. Marnier, C. Keller, L. Taleb, Tensile prestrain memory effect on subsequent cyclic behavior of FCC metallic materials presenting different dislocations slip modes, International Journal of Plasticity. 78 (2016) 64–83. https://doi.org/10.1016/j.ijplas.2015.11.001.

[52] C.-H. Yu, A. Leicht, V. Luzin, M. Busi, E. Polatidis, M. Strobl, R. Lin Peng, J.J. Moverare, Effect of Stress Relief Heat Treatment on Low Cycle Fatigue Behaviours of Lpbf Stainless Steel 316l, (2022). https://doi.org/10.2139/ssrn.4159502.

[53] G. Marnier, C. Keller, L. Taleb, Fatigue of OFHC pure copper and 316L stainless steel subjected to prior tensile and cyclic prestrains, International Journal of Fatigue. 91 (2016) 204–219. https://doi.org/10.1016/j.ijfatigue.2016.06.009.

[54] G. Marnier, Etude des effets de mémoire de pré-écrouissage affectant le comportement mécanique cyclique de matériaux métalliques présentant différents modes de glissement des dislocations, phdthesis, INSA de Rouen, 2016. https://tel.archives-ouvertes.fr/tel-01480227 (accessed March 31, 2022).

[55] J. Pegues, M. Roach, R. Scott Williamson, N. Shamsaei, Surface roughness effects on the fatigue strength of additively manufactured Ti-6Al-4V, International Journal of Fatigue. 116 (2018) 543–552. https://doi.org/10.1016/j.ijfatigue.2018.07.013.

[56] H. Hu, Y. Li, T. Suo, F. Zhao, Y. Miao, P. Xue, Q. Deng, Fatigue behavior of aluminum stiffened plate subjected to random vibration loading, Transactions of Nonferrous Metals Society of China. 24 (2014) 1331–1336. https://doi.org/10.1016/S1003-6326(14)63196-4.

[57] J. Zhang, A. Fatemi, Surface roughness effect on multiaxial fatigue behavior of additive manufactured metals and its modeling, Theoretical and Applied Fracture Mechanics. 103 (2019) 102260. https://doi.org/10.1016/j.tafmec.2019.102260.

[58] M.R. Bayoumi, A.K. Abdellatif, Effect of surface finish on fatigue strength, Engineering Fracture Mechanics. 51 (1995) 861–870. https://doi.org/10.1016/0013-7944(94)00297-U.

[59] J. Bruns, A. Zearley, T. George, O. Scott-Emuakpor, C. Holycross, Vibration-Based Bending Fatigue of a Hybrid Insert-Plate System, Exp Mech. 55 (2015) 1067–1080. https://doi.org/10.1007/s11340-015-0004-6.

[60] A.C. Grigorescu, P.-M. Hilgendorff, M. Zimmermann, C.-P. Fritzen, H.-J. Christ, Cyclic deformation behavior of austenitic Cr–Ni-steels in the VHCF regime: Part I – Experimental study, International Journal of Fatigue. 93 (2016) 250–260. https://doi.org/10.1016/j.ijfatigue.2016.05.005.

[61] H.H. Hausner, Powder characteristics and their effect on powder processing, Powder Technology. 30 (1981) 3–8. https://doi.org/10.1016/0032-5910(81)85021-8.

[62] A.T. Sutton, C.S. Kriewall, M.C. Leu, J.W. Newkirk, Powder characterisation techniques and effects of powder characteristics on part properties in powder-bed fusion processes, Virtual and Physical Prototyping. 12 (2017) 3–29. https://doi.org/10.1080/17452759.2016.1250605.

[63] T. Voisin, J.-B. Forien, A. Perron, S. Aubry, N. Bertin, A. Samanta, A. Baker, Y.M. Wang, New insights on cellular structures strengthening mechanisms and thermal stability of an austenitic stainless steel

fabricated by laser powder-bed-fusion, Acta Materialia. 203 (2021) 116476. https://doi.org/10.1016/j.actamat.2020.11.018.

[64] P. Krakhmalev, G. Fredriksson, K. Svensson, I. Yadroitsev, I. Yadroitsava, M. Thuvander, R. Peng, Microstructure, Solidification Texture, and Thermal Stability of 316 L Stainless Steel Manufactured by Laser Powder Bed Fusion, Metals. 8 (2018) 643. https://doi.org/10.3390/met8080643.

[65] R.R. Dehoff, M.M. Kirka, W.J. Sames, H. Bilheux, A.S. Tremsin, L.E. Lowe, S.S. Babu, Site specific control of crystallographic grain orientation through electron beam additive manufacturing, Materials Science and Technology. 31 (2015) 931–938. https://doi.org/10.1179/1743284714Y.0000000734.

[66] Fomin, Probabilistic fatigue-life assessment model for laser-welded Ti-6Al-4V butt joints in the high-cycle fatigue regime - ScienceDirect, (n.d.). https://www.sciencedirect.com/science/article/pii/S0142112318302305 (accessed March 31, 2022).

[67] Hu, The effect of manufacturing defects on the fatigue life of selective laser melted Ti-6Al-4V structures - ScienceDirect, (n.d.). https://www.sciencedirect.com/science/article/pii/S0264127520302422 (accessed March 31, 2022).

[68] I. Serrano-Munoz, J.-Y. Buffiere, R. Mokso, C. Verdu, Y. Nadot, Location, location & size: defects close to surfaces dominate fatigue crack initiation, Sci Rep. 7 (2017) 45239. https://doi.org/10.1038/srep45239.

[69] L. Liu, Q. Ding, Y. Zhong, J. Zou, J. Wu, Y.-L. Chiu, J. Li, Z. Zhang, Q. Yu, Z. Shen, Dislocation network in additive manufactured steel breaks strength–ductility trade-off, Materials Today. 21 (2018) 354–361. https://doi.org/10.1016/j.mattod.2017.11.004.

[70] P. Merot, F. Morel, L. Gallegos Mayorga, E. Pessard, P. Buttin, T. Baffie, Observations on the influence of process and corrosion related defects on the fatigue strength of 316L stainless steel manufactured by Laser Powder Bed Fusion (L-PBF), International Journal of Fatigue. 155 (2022) 106552. https://doi.org/10.1016/j.ijfatigue.2021.106552.

[71] X. Ni, D. Kong, W. Wu, L. Zhang, C. Dong, Deformation-induced martensitic transformation in 316L stainless steels fabricated by laser powder bed fusion, Materials Letters. 302 (2021) 130377. https://doi.org/10.1016/j.matlet.2021.130377.